Engineering Geology 304 (2022) 106700

Contents lists available at ScienceDirect

Engineering Geology

journal homepage: www.elsevier.com/locate/enggeo

Pore size distribution evolution in pellets based bentonite hydration: Comparison between experimental and numerical results

Liliana Gramegna [a,*], Fabien Bernachy-Barbe [b], Frédéric Collin [a], Jean Talandier [c], Robert Charlier [a,*]

[a] Université de Liège, Département ArGEnCo - Géotechnique, Géomécanique et Géologie de l'Ingénieur, 4000 Liège 1, Belgium
[b] Université Paris-Saclay, CEA - Service d'Etude du Comportement des Radionucléides, 91191 Gif-sur-Yvette, France
[c] ANDRA - Agence Nationale pour la gestion des Déchets Radioactifs, 92298 Châtenay-Malabry, France

ARTICLE INFO

Keywords:
Bentonite
Experimental methods
Numerical Modelling
Pore structure distribution
Finite Element Method
Water transfer mechanism

ABSTRACT

Several nuclear waste disposal concept designs take advantage of bentonite based materials to seal underground galleries and shafts. Safety assessment and long-term predictions of the material behaviour have been the main objective of a number of experimental campaigns and of constitutive models development. All these studies have underlined that the multi-porosity bentonite structure affects undeniably the strongly coupled hydro-mechanical processes taking place during water saturation. Due to this, in recent years, many classic experimental tests on unsaturated soils have been performed in conjunction with multi-scale observation techniques (for instance MIP, i.e. mercury intrusion porosimetry analises). Despite the well-known limitations of such observation methods, they provide interesting quantitative measurements in terms of pore diameters families, which differ by several orders of magnitude, and their distribution with respect to different assemblies' types (namely pellets mixtures and compacted bentonite blocks). On the other hand, very few studies have been focusing on the role of such pore size distributions with respect to the hydro-mechanical response, both from an experimental and a numerical point of view. The aim of this paper is to present the experimental campaign and the numerical modelling strategy adopted to analyse the role of different pore size distributions characterising MX-80 bentonite in different forms (i.e. 32 mm pellets mixture, 7 mm pellets mixture and compacted sample surrounded by gap) with same overall dry density during isochoric hydration tests. Taking advantage of multisensor-equipped cells and post-mortem analyses and of the finite element code LAGAMINE, the hydro-mechanical response of these bentonite assemblies is examined. Experimental and numerical outcomes result in good agreement and provide complementary information regarding the features of each assembly type.

1. Introduction

Thanks to their high swelling capacity upon hydration, very low permeability in saturated conditions and radionuclide retention capacities, bentonite based materials are selected as the engineered barriers' main component in the context of nuclear waste geological disposal (Cui, 2017) (Pusch, 1979). In most of the concept designs for nuclear waste disposal, bentonite-based materials are used to seal underground galleries and shafts, as in the French CIGEO concept (Sellin and Leupin, 2014), (Delage et al., 2010). However, bentonite can also be placed in direct contact with the canisters containing nuclear waste, as in the case analysed within the EB experiment (Alonso et al., 2010). Especially this latter one is a typical case of the combined use of compacted bentonite blocks and bentonite granular material. If on one hand, most of the experimental studies and constitutive models have mainly focused on bentonite compacted blocks in the past (Wang et al., 2013 among many), investigations on high density bentonite pellets combined with powdered bentonite are gaining increasing interest (Molinero et al., 2017), (Dardé et al., 2018)(Liu et al., 2019; Liu et al., 2020a; Liu et al., 2020b; Z. Zhang et al., 2015), (Bernachy-Barbe et al., 2020). Pellets mixtures present evident advantages in terms of large volume emplacements and technological gaps reduction in underground galleries.

* Corresponding authors at: Université de Liège, Département ArGEnCo. Géotechnique - Bât. B52/3, Géomécanique et Géologie de l'Ingénieur - Quartier Polytech 1, allée de la Découverte 9, 4000 Liège 1, Belgium.
E-mail addresses: liliana.gramegna@uliege.be (L. Gramegna), fabien.bernachy-barbe@cea.fr (F. Bernachy-Barbe), F.Collin@uliege.be (F. Collin), jean.talandier@andra.fr (J. Talandier), robert.charlier@uliege.be (R. Charlier).

https://doi.org/10.1016/j.enggeo.2022.106700
Received 1 December 2020; Received in revised form 20 April 2022; Accepted 4 May 2022
Available online 11 May 2022

This is due to the use of pneumatic stowing techniques, which make the backfilling operation an easier and potentially robotized procedure, especially of interest around high-level radioactive waste (Alonso et al., 2010). The pore structure distribution of such pellet mixtures (resulting from the intrinsic nature of the assembly together with this emplacement technique) can affect the performance in terms of mechanic and hydraulic properties. This pore structure distribution is composed of very small pore diameter structures (micro-pores) (i.e. from high dry density pellets) and large pore diameter structures (macro-pores) (i.e. from the low dry density crushed pellets component). The analysis of the hydro-mechanical features evolution of pellet-mixtures upon hydration is challenging.

Consequentially, the goal of this paper is to take advantage of a combined experimental and numerical approach to study the effect of different pore structure distributions on mechanic and water transfer mechanisms for similar average dry density assemblies. Experimental tests performed on four distinct MX-80 assemblies with different initial pore structure distributions but similar sample dry density are presented (Baryla et al., 2018). The tests have been performed by CEA (Commissariat à l'Énergie Atomique et aux Énergies Alternatives) on MX80 pellet mixtures (7 mm and 32 mm pellet diameters are considered) and compacted block in multisensor-equipped cells in the context of the BEACON project (Sellin et al., 2020). These tests provide quantitative information on granular materials, which is not as exhaustive as the one available for compacted bentonite blocks.

Then, the numerical strategy takes advantage on the Barcelona Basic Model (Alonso et al., 1990), which is considered for the bentonite mechanical behaviour, on pressure dependence, adopted for some mechanical parameters, and on the double porosity model proposed by Dieudonné et al. (2017), selected for the water retention behaviour and water permeability evolution (Dieudonné et al., 2017). Although the heterogeneous initial pore structure distribution of the analysed samples is well-recognized, in the adopted numerical strategy the overall assemblies are described in the framework of continuum mechanics. With reference to the comparison of experimental results and numerical predictions at dismantling (i.e. dry density and water content distributions), this work allows determining the limits of numerical modelling simplifications with respect to real laboratory conditions and vice versa.

2. Materials and experimental method

The objective of this series of tests carried out at CEA is to investigate the re-saturation in isochoric conditions of four MX-80 bentonite samples presenting similar dry density but different initial pore-size structure distributions and hydration lengths. These tests are performed in controlled conditions. Although the heterogeneities in terms of dry density and water content are characterized only in a post-mortem way (in the final state of the experiment), the swelling pressure field development upon saturation (and heterogeneities) is assessed using an array of sensors at various spatial locations (Baryla et al., 2018). The considered assemblies are composed of MX-80 bentonite in different forms. The MX80 bentonite is a clay from Wyoming (USA) with high content of smectite (77%) with some inclusions of non-clayey minerals (Micas~1%, Quartz~8%, Gypsum~1%, Calcite~1%, Feldspars~12%) (Tang et al., 2008), (Molinero et al., 2017).

Test WP5_1B, C_1 and C_2 consider pellets and crushed pellets mixtures (MX-80 bentonite: Laviosa-MPC Expangel SP32) with respective proportion between 70/30 and 67/33 in dry mass (Table 1). The components are arranged to minimize macroscopic gradients by building layer by layer dense arrangements of pellets with a fraction of powder (obtained from crushed pellets) filling the inter-pellets gaps, not exceeding the target dry density of 1.52 Mg/m^3. Test C_6 concerns MX-80 bentonite powder compacted and placed in the cell with a radial gap partially filled with loose powder.

Test WP5_1B sample is composed of 32 mm-pellets and crushed pellets, with three layers of intact pellets (38÷39 pellets) and a fourth layer with lower number of split pellets (≈8 pellets) with a final sample height equal to 105.15 mm and diameter equal to 240 mm. The dry density for one pellet is between 2.01 and 2.05 Mg/m^3 and initial water content w ≈ 4.04%, whereas crushed pellets present a particle size between 0 and 2.5 mm and w ≈ 4.55% (Talandier, 2018) (Fig. 1). The initial water content of the total assembly is equal to 4.23%. The sample to pellet diameter ratio (D/d) and sample height to pellet diameter ratio (H/d) are respectively equal to 7.5 and 3.3. Further information concerning this pellet size can be found in (Bernachy-Barbe et al., 2020).

Tests C_1 and C_2 are carried out on 7 mm-pellets/powder mixes. The dry density for one 7 mm-pellet is approximately 2.10 Mg/m^3 with initial water content equal to 5.07%. Further details concerning the 7

Table 1
Initial state and characteristics of the experimental and numerical samples.

TESTS	WP5_1B		C_1		C_2		C_6	
	Exp	Num	Exp	Num	Exp	Num	Exp	Num
Type of sample	32 mm pellets & crushed pellets	Homogeneous porosity	7 mm pellets & crushed pellets	Homogeneous porosity	7 mm pellets & crushed pellets	Homogeneous porosity	Compacted block & loose powder	Homogeneous porosity
Diameter [mm]	240		57		57		57	
Surface [cm^2]	452.39		25.52		25.52		25.518	
Height after adjustment [mm]	105.15	105.15 (Constant)	45	45 (Constant)	45.2	45 (Constant)	45.8	45 (Constant)
Volume after adjustment [cm^3]	4756.9	4756.88 (Constant)	114.83	114.83 (Constant)	115.34	114.83 (Constant)	116.87	114.83 (Constant)
Pellets [% mass]	69.9	[–]	66.9	[–]	66.9	[–]	[–]	[–]
Crushed pellets [% mass]	30.1	[–]	33.1	[–]	33.1	[–]	[–]	[–]
Clay density [Mg/m^3]	2.78		2.78		2.78		2.78	
Total porosity [%]	45.3	45.3	46	45.3	46.4	45.3	45.3	45.3
Pore volume [cm^3]	2156	2154.8	52.87	52.02	53.52	52.02	52.97	52.02
Water content [%]	4.23		6.65		6.81	6.65	7.44	
Saturation [%]	14.19		21.6	22.32	21.8	22.32	25.02	24.98
Initial average suction measured by cell sensors [MPa]	171.6	171.00 (Imposed)	161.3	115.00 (Imposed)	91.6	115.00 (Imposed)	75.7	100.00 (Imposed)
Bulk density [Mg/m^3]	1.58		1.6	1.62	1.59	1.62	1.63	
Dry density [Mg/m^3]	1.52		1.5	1.52	1.49	1.52	1.52	
Water volume to saturation [cm^3]	1849.03	1848.88	41.5	40.41	41.91	40.41	39.72	39.03

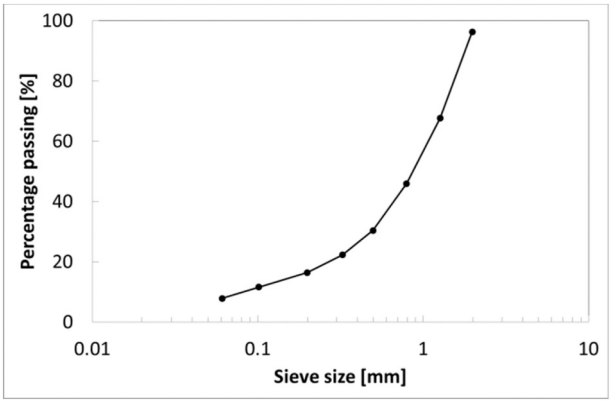

Fig. 1. Grain size distribution of the crushed pellets powder for test WP5_1B, C_1, C_2 and C_6.

mm pellets features can be found in (Molinero et al., 2017). The crushed pellets present the same granulometry curve as the one of test WP5_1B and initial water content w ≈ 10.33%. The initial dry densities of tests C_1 and C_2 are respectively equal to 1.50 mg/m^3 and 1.49 Mg/m^3, with initial water content equal to w ≈ 6.65% and w ≈ 6.81% and samples heights equal to 45.02 mm and 45.23 mm and diameter equal to 57 mm. The sample to pellet diameter ratio (D/d) and sample height to pellet diameter ratio (H/d) are respectively equal to 8.1 and 6.4 (twice as WP5_1B H/d ratio).

Test C_6 concerns MX-80 bentonite sample isotropically compacted at initial dry density equal to ρ_d = 1.75 g/m^3 and water content w = 7.44%. In order to perform the isotropic compaction, the clay was first compacted in a neoprene tube (90 mm in diameter, 120 mm in length and 1.2 mm in thickness) with a closed end. The sample within the tube was then compressed in an isotropic cell under a static pressure of 40 MPa and finally machined in order to fit the cell dimensions to a height equal to 45.82 mm and diameter equal to 52.8 (versus a cell diameter equal to 57 mm). The sample is placed in the cell with a radial gap partially filled with 3.35 g of loose powder (w = 7.44%) in order to obtain an overall final dry density equal to ρ_d = 1.52 Mg/m^3. The powder selected for the compaction of the sample and to fill the gap is the same as the one adopted for tests WP5_1B, C_1 and C_2. The addition of loose powder in the gap was used to adjust density and to avoid as much as possible instantaneous flooding of the gap by water. Experimental sample specifications can be found in Fig. 2 and Table 1. Further details with respect to tests conditions for tests C_1, C_2 and C_6 can be found in (Bernachy-Barbe, 2020).

Moreover, the three assemblies evidently differ in terms of pore volume distribution. Namely, pellet mixtures are characterized by very small diameter pore structure of the order of 0.02 μm represented by the high density pellets (micro-structure) and quite large diameter pore structure of the order of 100 μm given by the inter-pellets loose powder (macro-structure) (Molinero et al., 2017). On the other hand, compacted bentonite samples of similar overall dry density present the small diameter pore structure equal to 0.01 μm (micro-structure) and the large diameter pore structure of the order of 15 μm (macro-structure) (Seiphoori et al., 2014). Evidently, the pellet mixtures and compacted blocks bentonites mostly differ for the macro-structure diameters of at least 1 order of magnitude larger in the case of pellet assemblies.

The experimental devices consist of constant volume cells described in detail in (Imbert and Villar, 2006) and are not fully recalled here. Sensors measure axial force and displacements, radial total pressure and relative humidity at several levels. Water columns and tanks are placed on a continuous weighing device. Hydration is allowed with a slight differential pressure. Synthetic site water (described in (Bernachy-Barbe et al., 2020)) is injected with a very small hydraulic head (100 cm for test WP5_1B and 60–70 cm for tests C_1, C_2 and C_6) through porous plates on the bottom side (and/or the upper side) of the chamber, blocked at approximately zero displacement. In the case of unilateral hydration, the other side is placed at laboratory conditions to ensure evacuation of entrapped air. Two different diameters multi-equipped-sensor cells are used. The device selected for test WP5_1B presents a cell diameter equal to 240 mm and it is equipped with four radial pressure sensors and five relative humidity/temperature sensors at 20, 40, 60, 80 and 100 mm from the bottom face of 7.6 mm in diameter (Fig. 3).

Tests C_1, C_2 and C_6 are carried out in a smaller multi-sensor oedometric cell of diameter 57 mm equipped with 9 pressure sensors (total pressure or interstitial pressure) at 3 vertical positions (6.6 mm, 23.3 mm and 40 mm) and angular positions (0°, 90° and 180°) (Fig. 4). These sensitive elements are 7.6 mm in diameter. Three thermo-hygrometers are positioned at 270° and the same vertical positions as the pressure sensors.

3. Coupled hydro-mechanical model

3.1. BBM mechanical model

The complexity of the coupled multi-physical and multi-scale phenomena taking place during bentonite hydration is well known. The Barcelona Basic Model (BBM) (Alonso et al., 1990) is able to reproduce a wide range of phenomena occurring in unsaturated soils and, due to this, it is selected as mechanical constitutive model. The model is formulated adopting net stress $\boldsymbol{\sigma}$ (Eq. 1) and suction s as stress variables.

$$\boldsymbol{\sigma} = \boldsymbol{\sigma}_T - u_a \boldsymbol{I} \tag{1}$$

With $\boldsymbol{\sigma}_T$ the total stress tensor, u_a the air pressure for $s > 0$ and $\boldsymbol{I}$ the identity tensor.

According to the BBM, under isotropic stress conditions, the variation of volumetric elastic strain is associated to changes in mean net stress p and suction s (Eq. (2)). Moreover, in order to tackle the stress dependence of the swelling strain for change in suction underlined by (Dueck and Nilsson, 2010) Eq. (3) is adopted. The model parameters are described in Table 2.

$$d\varepsilon_v^e = \frac{\kappa}{1+e}\frac{dp}{p} + \frac{\kappa_s}{1+e}\frac{ds}{s+u_{atm}} \tag{2}$$

$$\kappa_s(p) = \kappa_{s0}{}^{*} exp\left(-\alpha_p{}^{*} p\right) \tag{3}$$

The evolution of the preconsolidation pressure $p_0(s)$ is modelled consistently with the concept of increasing the elastic domain with increasing suction (Eq. (4)) as well as the rate of increase of the soil stiffness with suction (Eq. (5)).

$$p_0(s) = p_c\left(\frac{p_0^{*}}{p_c}\right)^{\frac{\lambda(0)-\kappa}{\lambda(s)-\kappa}} \tag{4}$$

$$\lambda(s) = \lambda(0)[(1-r)exp(-\omega s) + r] \tag{5}$$

3.2. Double porosity hydraulic model

The selected water retention model (Dieudonné et al., 2017) is formulated in terms of water ratio e_w as a function of void ratio e and saturation degree S_r (Eq. (6)), which is expressed as the superposition of a contribution from the water stored in the micro-pores e_{wm} and a second contribution from the water contained in the macro-pores e_{wM} (Eq. (7)). (Dieudonné et al., 2017) bases the necessary distinction between micro and macro porosity on experimental observations and theoretical analyses performed in (Romero et al., 2011).

$$e_w = S_r e \tag{6}$$

$$e_w = e_{wm} + e_{wM} \tag{7}$$

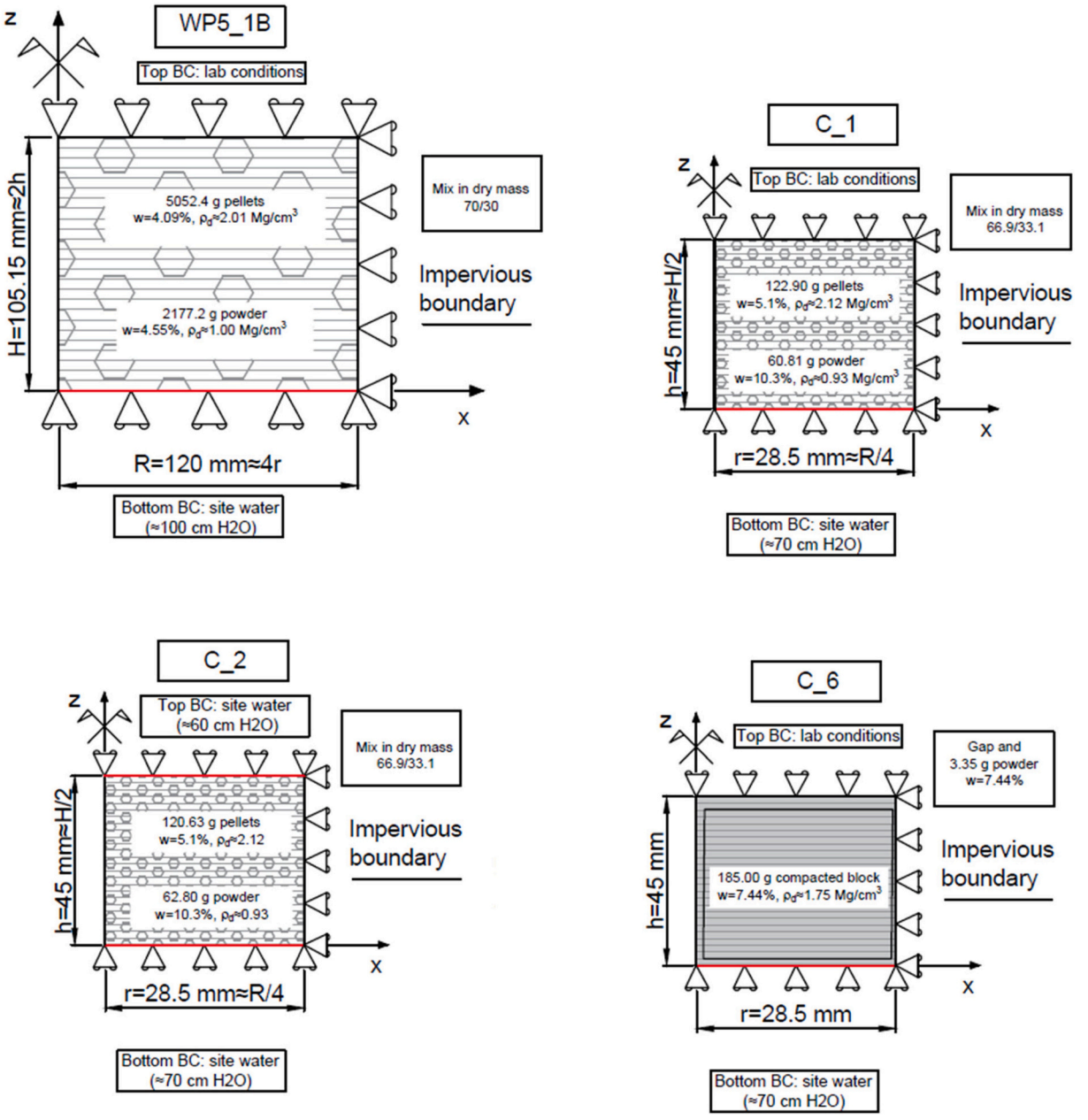

Fig. 2. Characteristics of the considered samples and boundary conditions of the model.

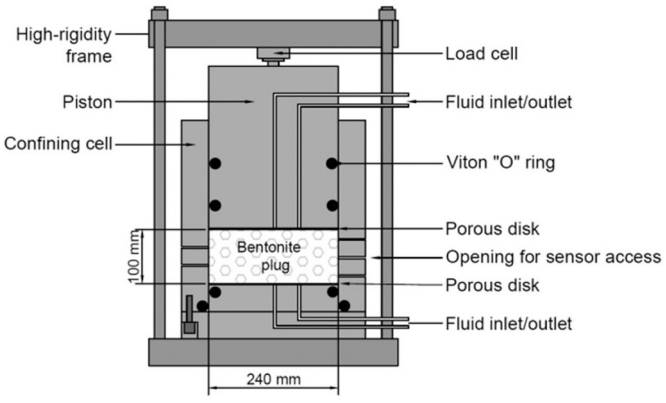

Fig. 3. Schematic representation of the experimental set-up of test WP5_1B.

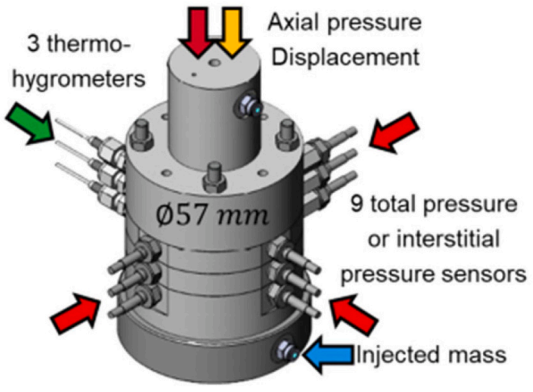

Fig. 4. Schematic representation of the experimental set-up of tests C_1, C_2 and C_6.

Table 2
Parameters of the mechanical model.

Test			WP5_1B	C_1 - C_2	C_6
κ	[−]	Elastic compressibility coefficient for changes in mean net stress	0.06	0.06	0.03
κ_s	[−]	Elastic compressibility coefficient for changes in suction	0.07	0.08	0.220
α_p	[−]	Parameter controlling the stress dependency of the swelling strain for change in suction	2.6×10^{-7}	2.6×10^{-7}	3.5×10^{-7}
p_0*	[MPa]	Pre-consolidation pressure for saturated state	1.86	1.86	0.3
p_c	[MPa]	Reference pressure controlling the shape of the LC curve	0.93	0.93	0.086
λ(0)	[−]	Slope of the saturated virgin consolidation line	0.20	0.20	0.25
r	[−]	Parameter defining the minimum soil compressibility	0.75	0.75	0.32
ω	[Pa]	Parameter controlling the soil stiffness	1.00×10^{-7}	1.00×10^{-7}	0.51×10^{-7}
φ	[°]	Friction angle	25	25	20
ν	[−]	Poisson ratio	0.35	0.40	0.17
c(0)	[MPa]	Cohesion in saturated conditions	0.10	0.10	0.10
k	[−]	Parameter controlling the increase of cohesion of increase of suction	0	0	0.0046

The model also considers the microstructure evolution occurring during saturation (Dieudonné et al., 2017) (Eq. (8)). Model parameters description is given in Table 3.

$$e_m = e_{m0} + \beta_0 e_w + \beta_1 e_w^2 \tag{8}$$

Therefore, the global degree of saturation is obtained by the sum of the microstructural and macro-structural degrees of saturation, weighed by the corresponding volumetric fractions (Eq. 9).

$$S_r = \frac{e_w}{e} = \frac{e_m}{e} S_{rm} + \frac{e_M}{e} S_{rM} \tag{9}$$

Dubinin's isotherm is adopted to describe the water retention behaviour of the microstructure, which is mainly stored by absorption (Eq. (10)). For the macro-structural water retention domain, the van Genuchten equation is selected (Eq. (11)) replacing the void ratio e by macro-structural void ratio $e_M = e\text{-}e_m$. The parameter α is assumed to depend on the macro-structural void ratio representing the influence of the bentonite structure on the air-entry value (Eq. (12)).

$$e_{wm}(s, e_m) = e_m exp[-(C_{ads} s)^{n_{ads}}] \tag{10}$$

$$e_{wM}(s, e) = (e - e_m)\left[1 + \left(\frac{s}{\alpha}\right)^n\right]^{-m} \tag{11}$$

$$\alpha = \frac{A}{e - e_m} \tag{12}$$

In order to consider the double structure nature of compacted bentonite-based materials also in the water transfer mechanisms, the water permeability evolution is modelled considering an Extended Kozeny-Carman model (Eq. (13)) similar to (Romero, 2013), in which the total porosity of the original model is substituted by the macro-void ratio e_M in the adopted one. In this way, the experimentally observed evolution of the larger pores will induce a reduction of the permeability.

$$K_w = C_k \frac{e_M^{expn}}{(1 - e_M)^{expm}} \tag{13}$$

A relative permeability law evolution is considered in this analysis (Eq. (14)), which reads:

$$k_r = S_r^{\gamma} \tag{14}$$

3.3. Geometric configuration and material parameters

The bentonite samples are numerically modelled with 25 eight-noded isoparametric elements. The problem is assumed mono-dimensional and oedometer conditions are considered (Fig. 2). Differences between the complex initial pore structure distributions of the 3 assemblies are well-recognized. They consist in small diameter pore structures, given by the pellets and compacted block (high dry density) and large diameter pore structures composing crushed pellets and gaps space filled with loose powder (low dry density). With respect to tests WP5_1B, C_1 and C_2, those structures and dry densities are randomly positioned inside the samples due to the casting technique, whereas in test C_6 the largest pore structures are mainly placed between the highly compacted bentonite sample and the cell wall in the radial direction.

For sake of simplicity, these distinctions are not considered in this work. Thus, initial uniform dry density equal to $\rho_d = 1.52$ Mg/m^3 is considered for all the four tests (considering the similar initial dry density in the experimental tests). Same hydro-mechanical properties and hydro-mechanical state are set with initial uniform suction s related to the saturation degree S_r, (obtained by the corresponding water content w and $\rho_d = 1.52$ Mg/m^3) via the adopted dry density dependent water retention model (Table 3).

The mechanical parameters (Table 2) for test WP5_1B, C_1 and C_2 were derived from the experimental campaign performed by (Molinero et al., 2019) on a similar assembly of MX80 pellets mixture and for test C_6 from the experimental campaign performed by (Tang et al., 2008) on MX-80 bentonite samples compacted with the same procedure. Mechanical parameters such as the friction angle, Poisson ratio and cohesion are in general very difficult to measure during experimental campaigns on swelling unsaturated bentonites (especially with respect to pellets mixtures) and very few data are available. Due to this, a trial and error procedure was adopted to reproduce the target results in terms of the swelling pressure measurements presented in this work.

The selected double porosity dry density dependent water retention model does not distinguish the initial pore structure distributions of the considered assemblies, thus a unique set of parameters corresponding to the calibration proposed by (Dieudonné et al., 2017) for compacted MX-80 bentonite is selected (Table 3). Initial water contents w in the numerical model are equal to the ones experimentally measured at the initial state (Table 1).

One single retention curve is used for the four tests and three

Table 3
Parameters of the water retention curve model.

Test			WP5_1B	C_1 - C_2	C_6
e_{m0}	[−]	Microstructural void ratio for the dry material	0.31	0.31	0.31
β_0	[−]	Parameters quantifying the swelling potential of the aggregates	0.1	0.1	0.1
β_1	[−]		0.48	0.48	0.48
C_{ads}	[MPa^{-1}]	Parameter associated to the desaturation rate of the soil	0.0075	0.0075	0.0075
n_{ads}	[−]	Parameter controlling the WRC curvature in the high suction range	0.2	0.2	0.2
n	[−]	Material parameters	3	3	3
m	[−]		0.45	0.45	0.45
A	[MPa]	Parameter controlling the dependence of the air-entry pressure on the macro-structural void ratio	0.2	0.2	0.2

different materials. Then the initial suction is deduced from the retention curve. It is considered that the water ratio measurement is more accurate than the suction measurement. With respect to this modelling choice, the initial relative humidity (i.e. suction) of the numerical samples is different from the one measured at the initial stage of the corresponding test (Figs. 5 and 6). It is worth noting also that the initial saturation values differ between the model and the experiments due to the slightly different initial dry density taken in consideration.

The parameters for the water permeability evolution (Table 4 and Fig. 7) were calibrated by best-fitting the responses of the water intake time evolution for the three different assembly types, thus the model parameters differ because the water intake kinetics of the different samples are not identical. Consequentially, the model is validated by comparing the swelling pressure kinetics and final dry density and water content distributions.

The hydration of the sample is provided from the bottom face for tests WP5_1B, C_1 and C_6 (hydration boundary conditions specified in Fig. 2) and additionally from the top for test C_2, assuming a suction decrease from the initial value to the experimental boundary conditions occurring in 1000 s. The sample of test WP5_1B is subjected to an initial confining stress value of 0.02 MPa in the axial direction and 0.2 MPa in the radial one, whereas test C_1, C_2 and C_6 are subjected to 0.02 MPa of confining stress in both axial and radial directions.

4. Water intake

4.1. Experimental results

Fig. 8 shows the water inflow time evolution normalized with respect to the cell volume together with semi-logarithmic scale for time. This normalisation helps to compare different cell sizes (and stabilisation times) in terms of water inflow but not for the kinetics. For instance test WP5_1B presents a final water mass injection value equal to 1849 g, 30 times larger with respect to the final water quantity measured in test C_6. Tests WP5_1B, C_1 and C_2 present a final water inflow/cell volume ratio equal to 40%, with an unexpected increase and decrease of water inflow for test C_2 possibly related to the establishment of water flux between the bottom and top wetting surfaces. Test C_6 shows a water inflow/cell volume ratio equal to 60%, larger with respect to the other experimental tests and unexpected with respect to the initial saturation degree. Water intake stabilisation time scale is proportional with the square of the hydration length. Namely, test WP5_1B presents a hydration length equal to 105.15 mm, tests C_1 and C_6 approximately equal to 45 mm and test C_2 equal to 22 mm, due to the fact that it is hydrated from the top and bottom surfaces simultaneously.

These experimental results show that the water injection evolution for the 57 mm diameter cell (tests C_1, C_2 and C_6) is not as smooth and

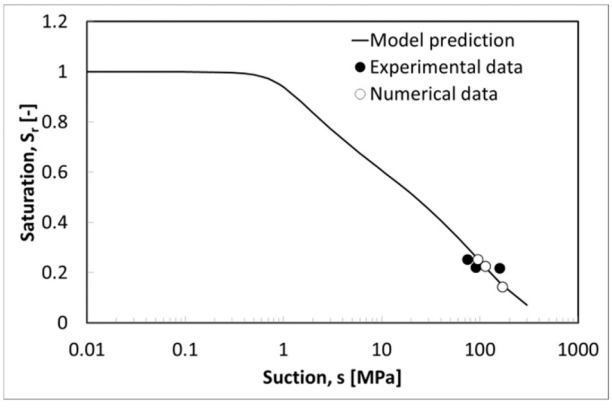

Fig. 5. Model prediction for the water retention curve. Initial experimental data and initial numerical data for tests WP5_1B, C_1, C_2 and C_6.

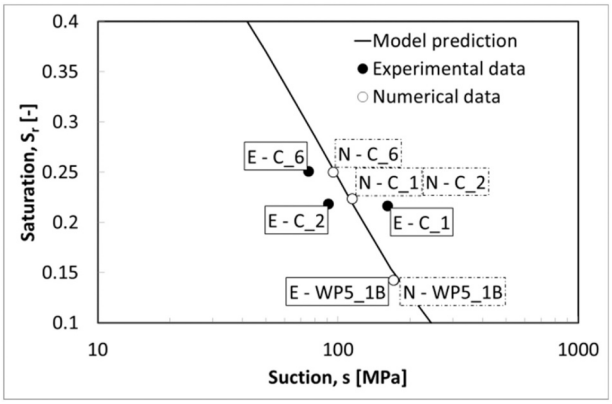

Fig. 6. Model prediction for the water retention curve. Initial experimental data and initial numerical data for tests WP5_1B, C_1, C_2 and C_6. Suction s between 10 and 1000 MPa and Saturation degree between 0.10 and 0.40.

Table 4
Parameters of the permeability evolution model.

Test			WP5_1B	C_1 - C_2	C_6
C_k	[m^2]	Reference permeability	1.8 $\times 10^{-20}$	1.8 $\times 10^{-20}$	1.8 $\times 10^{-20}$
expm	[−]	Model parameters	1.5	1.5	0.4
expn	[−]		0.2	0.4	0.4
γ	[−]	Parameter controlling the evolution of relative permeability	4	3	2

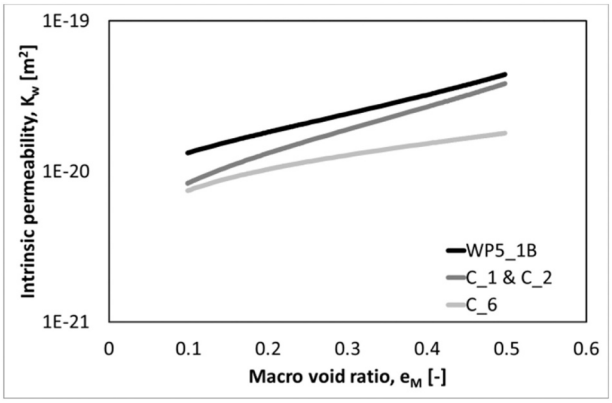

Fig. 7. Intrinsic permeability evolution with macro-void ratio accordingly to Eq. (13) and Table 4.

monotonic as the one related to the 240 mm diameter cell (Fig. 8 and Fig. 9). This can be related to the shorter experimental time scale, characterized by evident oscillations, but also to the difficulty to measure such small water quantities, which can undergo evaporation.

4.2. Numerical results

The permeability law evolution is calibrated on the experimental water intake time records for each type of assembly. Due to this, the numerical predictions for water intake evolution (Fig. 9) reproduce well the experimental results especially for test WP5_1B (32 mm-pellets mixture). With respect to 7 mm-pellets mixtures, it is interesting to note that for test C_1 (one side hydration) the numerical and experimental results do not coincide during the initial hydration phase. Namely, the experimental results underline a hydration process which is slower than

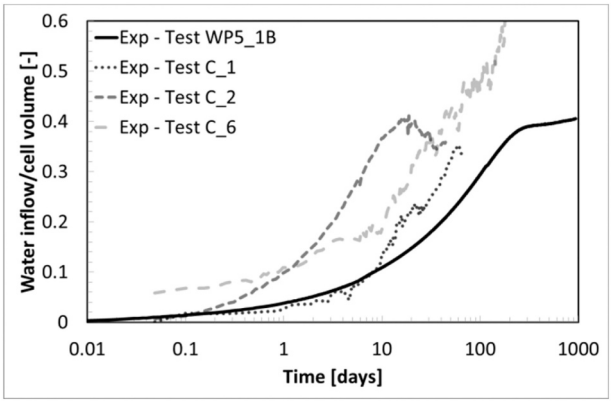

Fig. 8. Water mass injection time evolution divided by cell volume for tests WP5_1B, C_1, C_2 and C_6. Comparisons between experimental data.

the numerical one. On the other hand, numerical and experimental results for test C_2 (double side hydration) coincide well in the initial and final phases. Nevertheless, the numerical simulation of test C_2 does not reproduce the experimental increase and decrease of water inflow occurring between the 8th and the 30th days of the test.

For test C_6, the numerical and experimental water intake time evolutions correspond remarkably at the initial phase (i.e. until day 20), but an evident discrepancy in final values is observed. The numerical predictions are consistent with the initial experimental and numerical water contents, therefore, an experimental uncertainty is assumed.

For tests WP5_1b, C_1 and C_2, the numerical and experimental final water injection quantities are comparable as a consequence of similar initial saturation degrees. This result allows concluding that in terms of hydraulic properties the selected dry densities for tests C_1 and C_2 and sample dimensions for tests C_2 and C_6, which are slightly different between the experimental and numerical tests, do not affect remarkably the results.

5. Swelling pressure

5.1. Experimental results

Swelling pressures are measured axially. The axial total stress is considered uniform on each sample. The final axial swelling pressure values range between 3 MPa and 4.5 MPa, with the maximum value equal to 4.45 MPa recorded in test C_1 and the minimum equal to 3.27 MPa recorded for test C_2. While each sample presents about the same initial density and same initial water content, the final axial pressures differ evidently, which is unexpected and not predictable by most constitutive mechanical models. Tests C_1 and C_2 are the same type of assembly (i.e. 7 mm pellets mixture) with dry density $\rho_d = 1.50$ Mg/m^3 and $\rho_d = 1.49$ Mg/m^3 respectively. The dry density discrepancy between the two tests is equal to 0.67%, which does not justify a final axial swelling pressure discrepancy equal to 26%.

Axial swelling pressure experimental results of the four tests (Fig. 9 and Fig. 10) show similar pressure evolution with time. Three phases can be distinguished: an initial quick swelling pressure increase, a second phase with a slower increase, a change of curvature, and the last one with a new increase of the swelling pressure. Such features have already been described by (Imbert and Villar, 2006) with respect to FoCa bentonite granular mixtures. (Lloret et al., 2003) describe similar stress paths analysing the behaviour of compacted Febex bentonite subjected

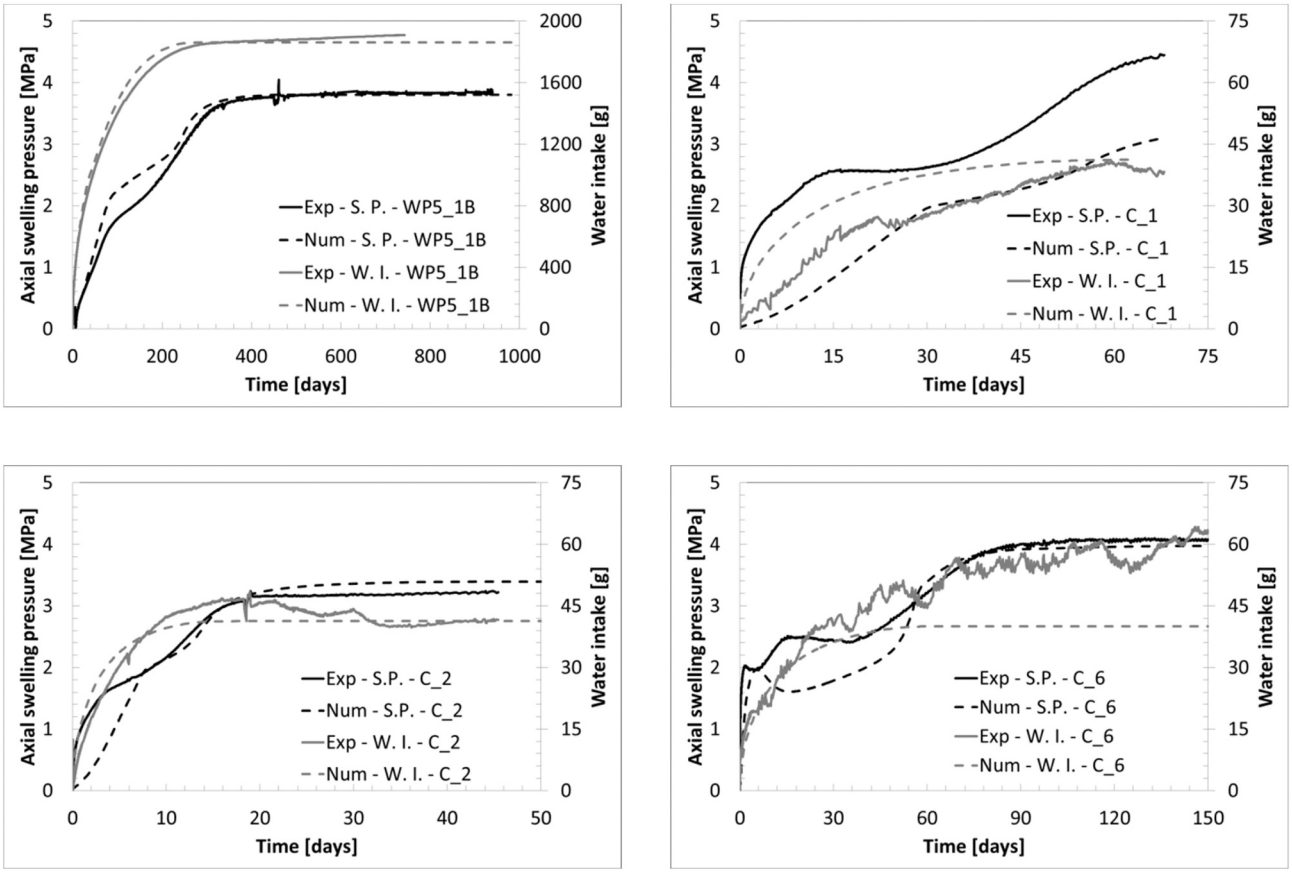

Fig. 9. Swelling pressure in axial direction and water mass injection time evolution for tests WP5_1B, C_1, C_2 and C_6. Comparisons between experimental data and model predictions.

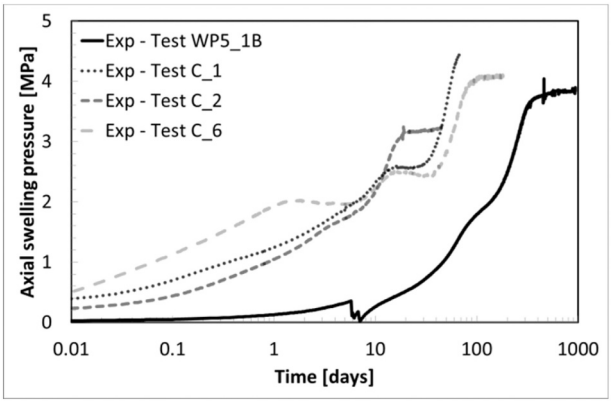

Fig. 10. Swelling pressure in axial direction time evolution for tests WP5_1B, C_1, C_2 and C_6. Comparison between experimental data.

to constant volume hydration with a special focus on the interaction between micro and macrostructure.

The first swelling pressure increase corresponds to the stage of high suction and low swelling pressure. In the framework of elasto-plasticity, the stress state has not reached the yielding surface. It can be assumed that the stress path is defined by the increase of load required to compensate the small swelling strains due to suction reduction. The elastic swelling pressure in the axial direction develops with higher rate in test C_6 (compacted bentonite sample) with respect to tests WP5_1B, C_1 and C_2. The second phase occurs after reaching the pre-consolidation pressure (yield locus), in which the stress paths encounter a drastic change of slope. According to (Lloret et al., 2003), the micro-structure can present a load sufficiently high to cause the collapse of the macro-structure, where the successive vertical stress decrease is due to the compensation for the collapse compressive strains. The micro-structural swelling strains contribute to the compensation for collapse deformation, and if it is large enough it can compensate the swelling pressure decrease. The third phase corresponds to the region of low suction and high saturation. In this range, the microstructural swelling strains exhibit their largest magnitude (Wang et al., 2013) and overcome any possible collapse strains. The stress increases again to compensate for the large swelling strains.

The radial total pressure measurements (Figs. 11 and 12) show variations with respect to the sensors position. The final average values range between 2.8 MPa and 4.8 MPa. Experimental radial pressure evolutions recorded by all the sensors are reported in (Bernachy-Barbe, 2021). It is important to mention that, during an experimental test, the radial pressure is more difficult to measure with respect to the axial one due to the fact that it is strongly affected by the test conditions and representative only of a limited portion of the sample. Moreover, recent studies (Cui, 2017; Darde et al., 2020) underline that the sensors area itself can affect the experimental outcome. Also the presence of a possible radial pressure gradient (i.e. longitudinal evolution of a given value for a given time through the height of the sample) has to be taken into account (particularly evident in test C_6). Consequentially, those values have to be treated and interpreted with caution.

The time evolution of the radial pressures is mostly similar to the axial pressure evolution with respect to the division into the above-mentioned phases.

High stress gradient through the height of the sample can be observed at early stages of hydration for compacted block test C_6, where the effect of the gap appears important. Indeed it can be observed

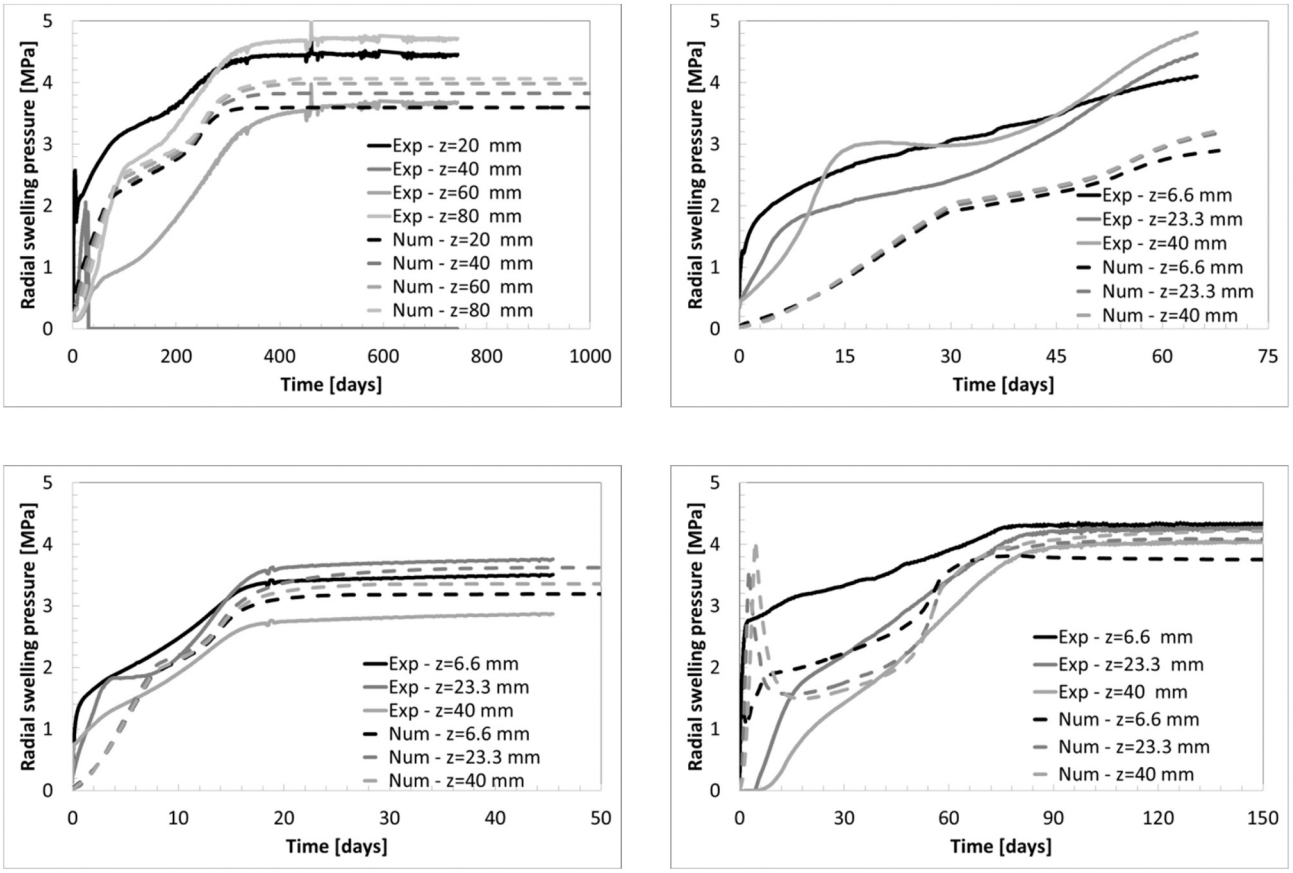

Fig. 11. Swelling pressure in radial direction at several locations time evolution for tests WP5_1B, C_1, C_2 and C_6. Comparisons between experimental average data and model predictions.

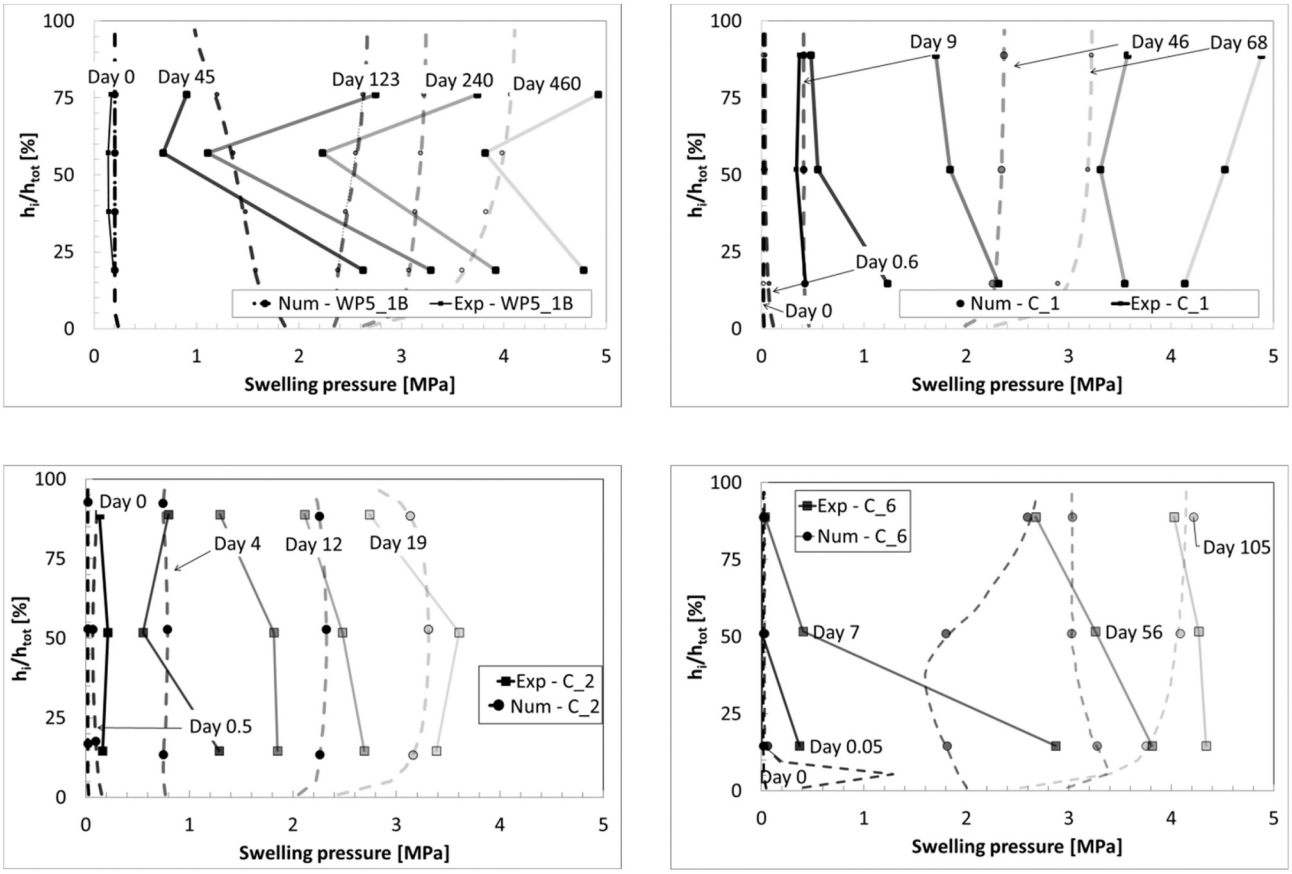

Fig. 12. Radial swelling pressure profiles for tests WP5_1B, C_1, C_2 and C_6. Comparison between experimental average measurements and numerical predictions. Time steps are selected considering the initial conditions, the 25%, 50%, 75% and 100% of the final experimental axial swelling pressure of each test.

in Fig. 12, that the sensors located at z = 40 mm from the bottom (h_i/h_{tot} = 89%) detects a null radial swelling pressure at the 7th day of the test time. At the same moment, the sensor at z = 6.6 mm (h_i/h_{tot} = 15%) presents a radial swelling pressure equal to 3 MPa. Thus, when the 60% of the total swelling pressure has already been developed, the radial contact has not been reached yet at the upper location. This means that hydration has highly developed at the bottom but not at the top of the sample.

The pellet/powder arrangements (tests WP5_1B, C_1 and C_2) do not show such high stress gradients. Surprisingly, there not a high difference in the radial pressure gradient between C_1, which is only hydrated by the bottom, and C_2, which is hydrated by the top and the bottom.

The hydration duration can be observed in Figs. 8 and 9. Test WP5_1B was stopped at 1214 days after the beginning of hydration, C_1 after 68 days, C_2 after 45 days and C_6 after 182 days, with pressure measurements for test WP5_1B, C_2 and C_6 stable respectively since approximately a duration of 600 days, 20 days and 80 days (test C_1 does not seem to reach stabilisation). It can be observed that the stabilisation times (i.e. time after which water intake increments become negligible) are proportional to the square of hydration length as observed for the water intake.

It is worth noting that the swelling pressure stabilisation is not consistent with the relative humidity (i.e. suction) measurements, which reach the 100% far earlier (see Section 6.1, Fig. 13). The first and fast increase of the pressures seems to follow the RH increase. The second swelling pressure increase arrives for low suction, when relative humidity is near 100%. Alternatively the swelling pressure development is more coherent with the water intake evolution (Figs. 8 and 9).

5.2. Numerical results

Figs. 9 and 11 show the time evolution of the swelling pressure measured in the axial direction on the top and in the radial one at different heights of the samples. The numerical results are compared to the experimental ones. The trend of the transient phase is well reproduced as well as the stabilisation time.

As the comparisons in Fig. 9 show, the agreement between the experimental and the numerical results for the axial pressure is remarkably good for test WP5_1B, C_2 and C_6. Discrepancies between model predictions and experimental results are found in test C_1, as the last increase is not reproduced. Given the same initial conditions in terms of confining stress and saturation, the same final swelling pressure is obtained in numerical simulations for tests C_1 and C_2. Indeed, apart from different stabilisation times proportional to the square of the hydration length equal to 45 mm for test C_1 (one side hydration) and 22.5 mm for test C_2 (double-sided hydration), the two numerical tests present the same final swelling pressure values equal to 3.2 MPa. This value is evidently lower with respect to the one observed during the experimental test C_1.

Moreover, differently from test WP5_1B, in which the initial elastic experimental swelling is remarkably well reproduced, test C_1 and C_2 present an elastic swelling pressure development delayed with respect to the experimental records. This occurrence can be related to the selection of the mechanical elastic parameters for change in pressure κ (constant) and for change in suction κ_s (pressure dependent). Hydraulic mechanisms dependence causes are excluded as it was explained in the previous paragraph.

On the other hand, the numerical post-yielding path for test C_2 is perfectly corresponding to the experimental measurements. The

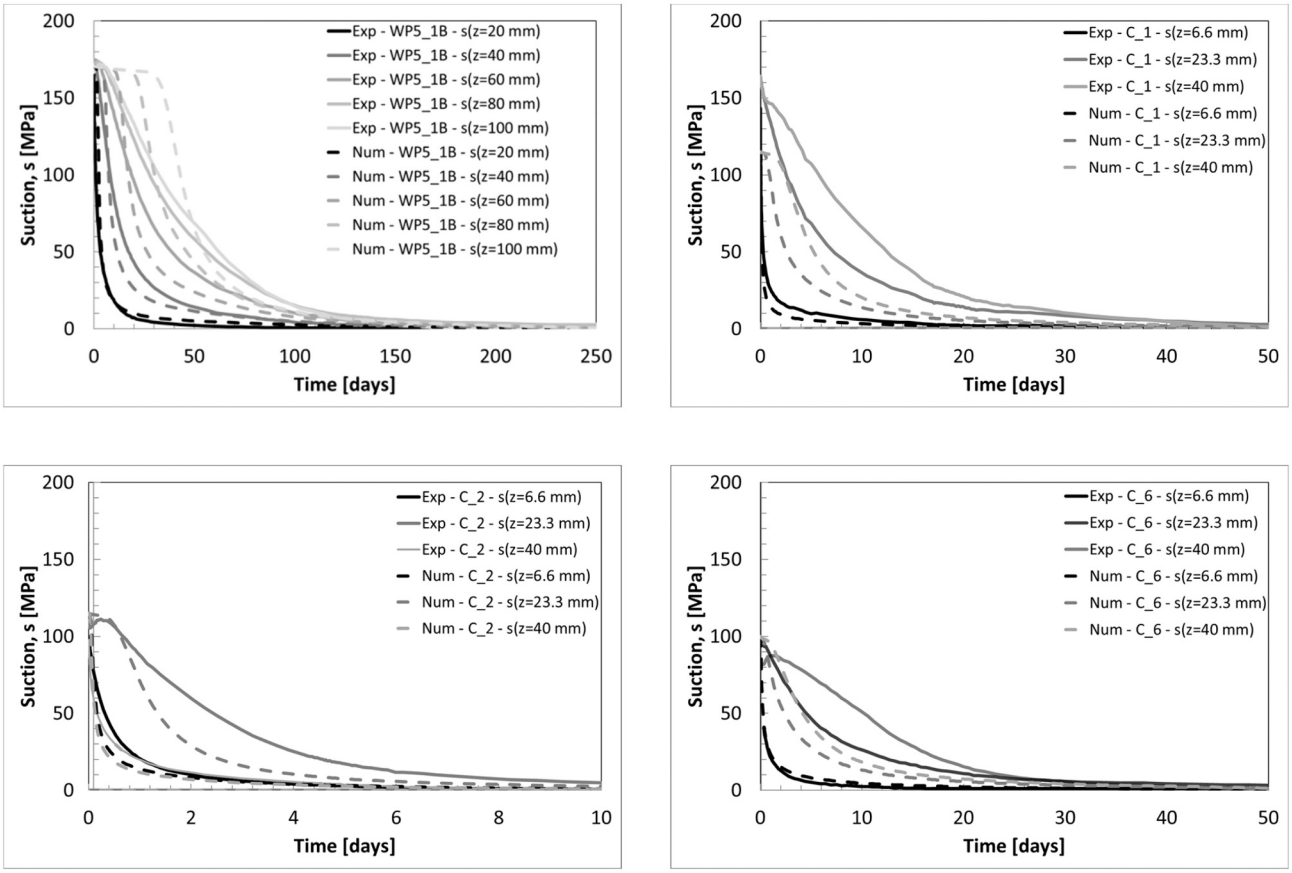

Fig. 13. Suction at several locations time evolution for tests WP5_1B, C_1, C_2 and C_6. Comparisons between experimental data and model predictions.

numerical prediction of axial swelling pressure for test C_6 is able to reproduce the path described by (Lloret et al., 2003) without explicitly taking into account the small-large diameter pores interaction but considering mono-modal pore distribution in the mechanical model (i.e. BBM).

The numerical swelling pressure developments and values differ in the three cases mostly due to the different mechanical parameters calibration and selection (Table 2).

Radial stress measurements comparisons are shown in Figs. 11 and 12. Numerical predictions present a pressure gradient in the hydration direction, with a maximum value for the sections further from the wetting surfaces. The non-monotonic evolution of the swelling pressure during the hydration phase is well captured by this model. However, numerical radial pressure predictions are in general lower than the averaged experimental ones and are not affected by local uncertainties. Indeed, the numerical radial stress distributions at the end of the tests (Fig. 12) preserve the developed pressure gradient, differently from experimental records. With respect to tests C_1 and C_2, numerical initial radial confining pressure is selected equal to 0.02 MPa, lower with respect to the measured quantities, which have to be treated with caution considering also the sensors precision and dimension (Dardé et al., 2019). The numerical predictions for the radial pressure evolution of test C_6 are similar to the axial ones (i.e. increase of pressure up to a peak followed by a decreasing and a final increase up to stabilisation), in contrast to what is observed in the experimental outcomes where the role of the initial gap is dominant. Since the numerical strategy considers mono-dimensional conditions, initial mono-modal pore structure distribution and no gap with the cell wall, this experimental evidence is not well-captured in this study. The very high initial radial pressure gradient observed during experimental results of test C_6 is indeed due to the radial gap.

6. Suction

6.1. Experimental results

As soon as the water injection begins, the suction decreases for all the heights in all the tests (Figs. 13 and 14). The rate of decrease is inversely proportional to the distance from the water source, with the maximum rate recorded at the sensors closest to the wetting surface. With respect to experimental tests WP5_1B, C_1 and C_2, at the beginning of the injection, water mostly flows into the bigger diameter pores composing the crushed pellets powder in which the sensors are immersed. Because of this, the suction immediately decreases. When the water front proceeds through the sample, the pellets hydrate and swell, compacting the surrounding powder. From a multi-structural point of view, pellets' dominating small diameter pore structure invades the crushed pellets large diameter one, preventing the local water transfer mechanism and consequentially slowing down the suction decrease. For test WP5_1B, the zero experimental suction values at all the sensors are reached at the test duration of day 200, when the swelling pressure reaches 65% of its total swelling pressure. Thus it can be concluded that at that time, the crushed pellets component is fully saturated, as RH sensors indicate, whereas the pellets component continues to hydrate, as the water intake evolution shows, still causing swelling pressure development until the age of day 400 when full saturation is assumed.

This latter occurrence is also found in tests C_1 and C_2 in which the zero suction values are obtained at the time of 50 and 10 days respectively, whereas the swelling pressures and water intake stabilise at the time of 70 and 20 days. However, the immediate water invasion of crushed pellets component is not as evident as the one observed in test WP5_1B.

Due to this it can be assumed that the suction measurements are not

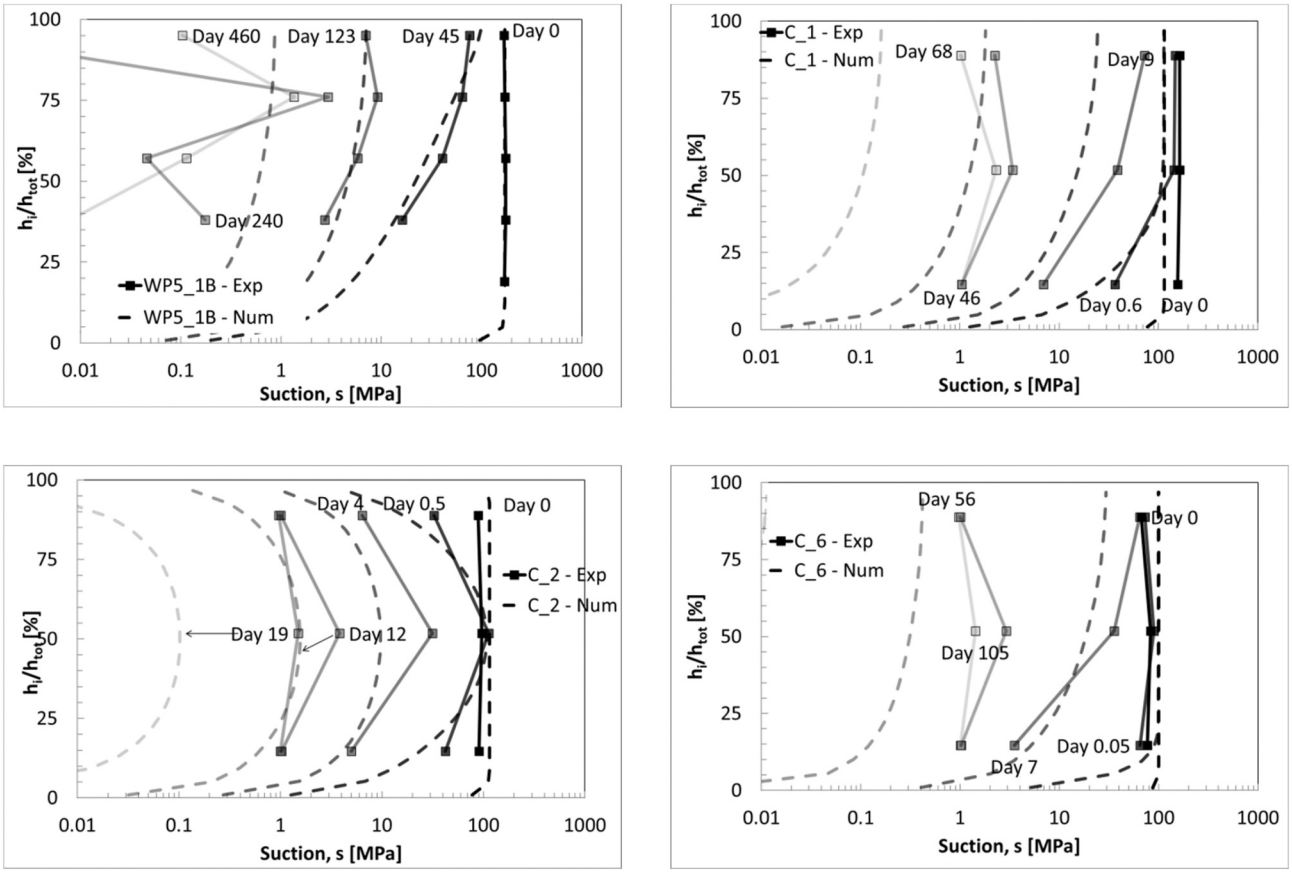

Fig. 14. Suction profiles for tests WP5_1B, C_1, C_2 and C_6. Comparison between experimental measurements and numerical predictions. Time steps are selected considering the initial conditions, the 25%, 50%, 75% and 100% of the final experimental axial swelling pressure of each test.

representative of the overall bentonite sample but mainly of the pore space corresponding to the crushed inter-layer pellets for tests WP5_1B, C_1 and C_2 and to the powder gap space for test C_6, i.e. to the larger pores. These measurements are local, in the same way as the radial pressure measurements, whereas the axial pressure and the water intake are global values. Fig. 14 presents the evolution with time of the vertical gradient of suction. WP5_1B and C_1 tests present similar tendency, consistently with powder material and only bottom hydration. A clear, almost uniform gradient appears for intermediate state of hydration (45 days for WP5_1B, 9 days for C_1). Test C_6 presents also the same trend. Test C_2 is hydrated from the top and bottom, and this is clearly reflected in the "chevron" shape of the suction profile. All these profiles at intermediate state of hydration are a signature of the permeability evolution of the materials at early stages.

6.2. Numerical results

The numerical model captures very well the progressive decrease in suction experimental measurements from the hydration surfaces to the opposite direction (Figs. 14 and 13). Moreover, the numerical results reproduce nicely the experimental profile at intermediate times (Fig. 14), when the suction is far from being uniform in the sample (at day 45, 9 and 0.5 for tests WP5_1B, C_1 and C_2 respectively). This shows that the model reproduces well the suction evolution. The best agreement between numerical and experimental results is found for measurements placed the closest to the wetting faces. The very fast reaction of these sensors is well reproduced numerically. Discrepancies are found for the sensors further from the injection fronts.

With respect to test WP5_1B, a quick experimental suction decrease for all the sensors is observed, which is not reproduced by the numerical model. Indeed, for the further sensors, at the beginning of the hydration, the numerical predictions display quasi-constant suction values, which start to evolve at a time proportional to the distance from the wetting surface. As the hydration process continues, the numerical suction dencrease rates overcome the experimental one up to full saturation.

Also for tests C_1 and C_2 the numerical model reproduces well the dencrease of suction for the sensors located closer to the wetting surfaces, with slightly higher numerical values with respect to the experimental ones (as observed for water intake comparisons). As the distance from the wetting surfaces increases, the rate of suction decrease is higher for the numerical model with respect to the experimental measurements. These discrepancies can be explained by analysing the important pore structure changes occurring during hydration described in the experimental analyses. Indeed, the numerical results show faster suction decrease rates with respect to the experimental ones, possibly suggesting a different pore structure evolution kinetic due to the different pellets size (7 mm-pellets instead of 32 mm).

Finally test C_6 suction comparison shows that also in this case the suction evolution is very well reproduced for the sensor at z = 6.6 mm (h_i/h_{tot} = 15%), where the contact between the sample and the cell immediately occurs. For the further sections, it is necessary to point out that during the experimental test, the suction starts to decrease due to the water hydration only after the establishment of the contact between the material and the sensors. In the numerical modelling, the suction evolution for the further sensors locations is not very well reproduced at the very beginning because initial contact is assumed and for the initial suction value, which is different from the experimental one.

The proposed numerical strategy does not consider such a complex pore structure distribution, its dramatic evolution upon hydration and the different saturation processes between small diameter pores

structures (pellets and compacted blocks) and large diameter pores structures (crushed pellets and gaps components), but it gives interesting hints in terms of pore structure evolution homogenisation and kinetics.

7. Permeability evolution

7.1. Experimental results

According to (Cui, 2017) the unsaturated permeability in bentonite based materials is undeniably linked to the multi-structures evolution upon hydration. Hence, in the specific cases of tests WP5_1B, C_1 and C_2, it can be assumed that the crushed pellets component, thanks to its structure dominated by large pores in the initial unsaturated state, represents a preferential pathway for the water transfer mechanism during the first phases of hydration. This feature results in a quite high initial permeability, which immediately decreases as the pellets swell and the small diameter structure expansion proceeds on wetting. This topic was also faced by (Navarro et al., 2020) with respect to test WP5_1B. In the same fashion, it can be considered that in test C_6 (i.e. compacted bentonite block), the water transfer mechanism takes mainly place in the largest diameter pores during the first phases of hydration with a permeability, which decreases as the larger diameter pore structure is invaded by the expansion of the small diameter pore structure upon saturation. Differently from pellets mixtures, it can be assumed that the compacted bentonite sample composing test C_6 does not present an initial permeability as high as the one postulated for test WP5_1B, C_1 and C_2 pellet mixtures. This is related to the fact that the very large pores size diameter characterising the crushed pellets medium is not likely in the compacted materials structure.

Moreover, it seems evident with respect to the water intake evolution, swelling pressure stabilisation and relative humidity (Figs. 8, 9, 11 and 13), that test C_6 (compacted bentonite block, which stabilises after more than 80 days) presents an average permeability slightly lower than the one related to tests C_1 (7-mm pellets mixture), despite the comparable initial hydraulic state and dry density.

7.2. Numerical results

It is important to underline that in media presenting heterogeneous pores size distributions, such as the ones here analysed, large pore diameter structures (i.e. the crushed pellets medium or gaps) are preferential (and possibly unique) hydration paths, especially at the beginning of the hydration process. Here, the water is free and behaves as a Darcean fluid (contrarily to what occurs in the small pore diameter structures). Fig. 15 shows the numerical permeability predictions profiles through the height of the samples.

The selected numerical model for the permeability evolution allows reproducing the permeability decrease due to the micro-structure evolution upon water saturation (Fig. 16). In all the studied cases (i.e. isochoric hydration), the micro-porosity becomes dominant with respect to the macro-porosity (i.e. inter aggregates and inter pellets pore space) upon water saturation according to Eq. 8. Due to this, starting from uniform values of intrinsic permeability (Table 4), obtained following Eq. (13) (Fig. 7) and depending on the saturation degree via e_M and k_r (Eq. (8) and Eq. (11)), as the water front proceeds from the wetting faces, the intrinsic permeability of the material decreases reaching a quasi-uniform value when fully saturated along the height of the samples (i.e., RH = 100%, Figs. 14 and 13 dashed lines).

As the hydration begins, the permeability of the material placed closest to the wetting faces immediately decreases as the large pore structures are invaded by the small pore one. Despite these portions of

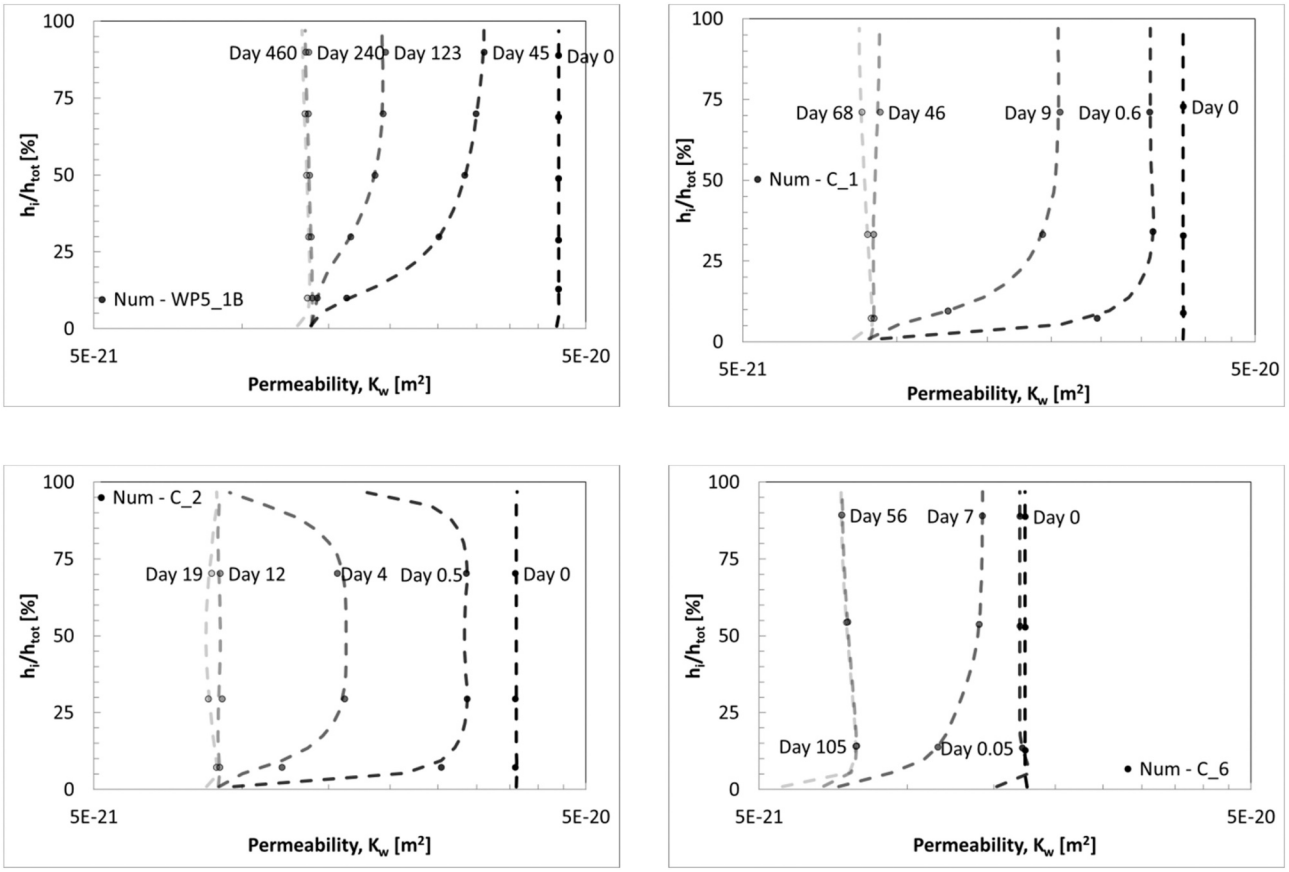

Fig. 15. Permeability profiles for several time steps. Numerical predictions for tests WP5_1B, C_1, C_2 and C_6.

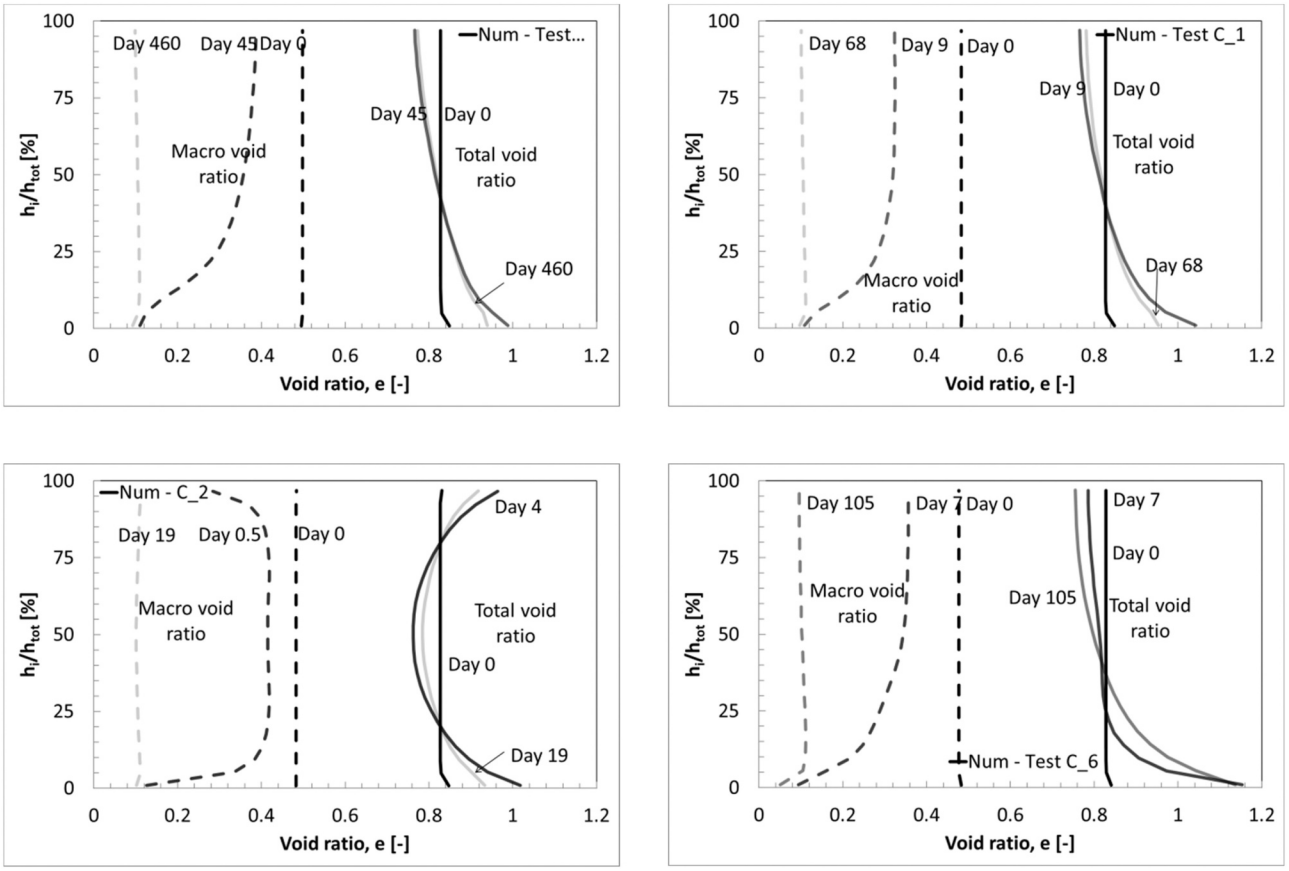

Fig. 16. Total and macro void ratios profiles for several time steps. Numerical predictions for tests WP5_1B, C_1, C_2 and C_6.

the samples being subjected to a generalized swelling (Fig. 17), which should correspond to a permeability increase, the large pore structures are instantly invaded by the micro pores structures causing the observed permeability decrease. This phenomenon is predominant with respect to other mechanisms and occurs in pellets mixtures, in which the powder/crushed pellets inter-pellets place (preferential path way of hydration) is compacted due to the pellets swelling, but also in the compacted block, in which the radial gap is invaded by the compacted sample swelling upon hydration in isochoric conditions (Seiphoori et al., 2014).

The initial and slower permeability decrease observed in the samples portions further from the wetting surfaces are initially related to the compaction caused by the bentonite swelling and successively by the multi-structural evolution, occurring in both experimental observations and numerical predictions. All these phenomena are linked to each other and testify the strong hydro-mechanical and multi-porosity coupled processes characterising unsaturated swelling clays.

These causes explain the observed RH rate decrease after the first and quicker hydration phase, confirming the hypothesis of water transfer mechanism mainly occurring in large pores diameter structures during the first phases of hydration.

The calibration performed for the 3 different assemblies shows the highest initial uniform permeability equal to $K_w = 4 \times 10^{-20}$ m^2 for 32-mm pellets mixture (test WP5_1B) and the lowest equal to $K_w = 8 \times 10^{-21}$ m^2 for the compacted sample (test C_6). Intermediate value equal to $K_w = 2 \times 10^{-20}$ m^2 for 7-mm pellets mixture (tests C_1 and C_2).

The final permeability values corresponding to the full saturated state are equal to $K_w \approx 6.5 \times 10^{-21}$ m^2 for 32-mm pellets mixture (test WP5_1B), $K_w \approx 5.5 \times 10^{-21}$ m^2 for the compacted sample (test C_6) and the 7-mm pellets mixtures (tests C_1 and C_2).

The permeability rate decrease upon saturation can be also observed in Fig. 7. Despite several simplifications adopted to model these experimental tests (i.e. unique water retention curve, different initial RH and macro void ratio e_M depending only on the saturation degree and not on effective pore structure distribution), the numerical model and its calibration are able to well reproduce the transient phase of swelling pressure development, RH evolution and dry density and water content final states (as it will be observed in the following) and give realistic results in terms of permeability evolutions.

8. Post mortem analyses

8.1. Experimental results on dry density and water content

Dry density and water content were evaluated thanks to post mortem analyses. Water content was measured using 105 °C oven drying for 24 h and the apparent density from hydrostatic weighing in oil. Consequentially, dry density is computed for each sub-sample. For test WP5_1B, six dry density measurements at four heights were taken. Dry density and water content results consider the mean and standard deviations, which underline a certain level of results dispersion (between $\rho_d = 1.47$ and 1.58 Mg/m^3) (Bernachy-Barbe et al., 2020). For tests C_1, C_2 and C_6, apparent density measurements (three for tests C_1 and C_2 and one for test C_6) and one water content measurement are taken at three locations through the vertical axis of the samples. The dry density measurements dispersion of tests C_1, C_2 and C_6 is much smaller with respect to test WP5_1B.

A vertical density gradient is observed in the direction of hydration, inversely correlated with water content (Figs. 17 and 18) for tests WP5_1B, C_1 and C_2. The minimum dry density values (maximum water content values) are found in the locations close to the wetting surfaces. When water is injected, the material placed close to the wetting surfaces undergoes an important volume increase. Accordingly to the

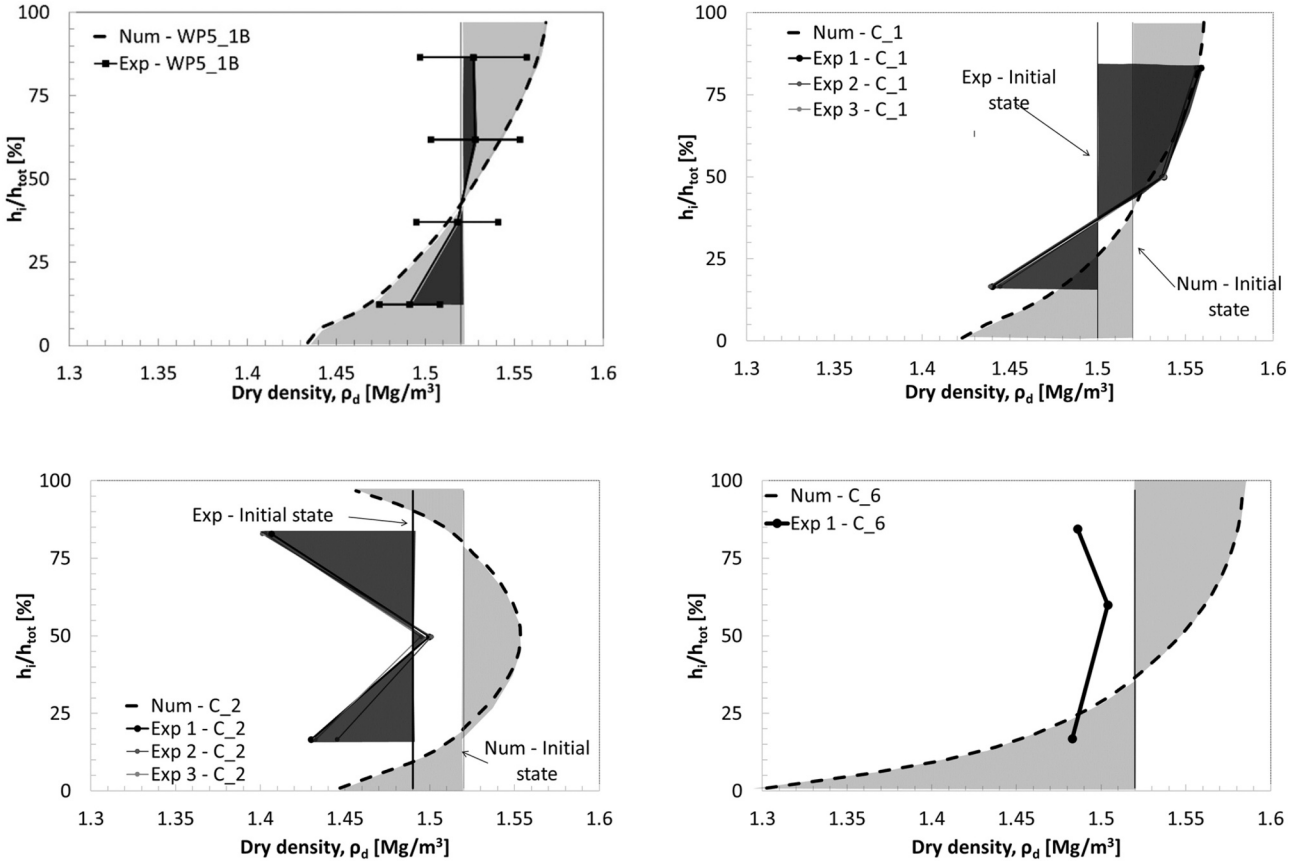

Fig. 17. Dry density distribution over the height of the sample (in percentage) at the beginning and the end of the test for tests WP5_1B, C_1, C_2 and C_6. Comparisons between experimental data and model predictions.

prescribed isochoric conditions, this volume increase should be counterbalanced by a volume decrease far from hydration front. Thus, this latter zone is compressed by the swollen of the wetted material. As the saturation front penetrated within the sample, the transition between the swollen and compressed zone recedes from the injection sides and stops before the first half of the hydration length (~45% h_i/h_{tot} from the wetting surface).

With respect to the experimental results related to test C_2 (Fig. 17), experimental outcomes underline a generalized volume increase, which contradicts the hypothesis of constant volume hydration.

On the other hand, the general decrease of dry density detected in the experiment can also be an artefact caused by swelling after dismantling or during sampling. Indeed, as observed for the numerical prediction of test C_2 final state, the central part presents a higher dry density with respect to the top and bottom parts (i.e. a gradient in the hydration direction).

Test C_6 shows a final homogeneous dry density (and water content) distribution between $\rho_d = 1.45$ and 1.50 Mg/m^3. (and $w = 30\%$). It is interesting to note that the initial dry density of the compacted block was equal to $\rho_d = 1.75$ Mg/m^3, with a swelling deformation, possibly occurred in the radial direction (i.e. the gap). Also in this case post dismantling and sampling swelling is assumed due to the fact that the overall final dry density is slightly lower with respect to the overall one ($\rho_d = 1.52$ Mg/m^3).

Samples composed of pellets mixtures present a larger density variation: 0.10 Mg/m^3 for WP5_1B, 0.12 Mg/m^3 for C_1 and for C_2.

8.2. Numerical results on dry density and water content

Dry density and water content comparisons of experimental measurements at dismantling and numerical results are presented (Figs. 17 and 18). For tests WP5_1B, C_1 and C_2, the final experimental and numerical states show similar qualitative features: a vertical density gradient is observed in the direction of hydration, inversely correlated with water content. The resulting vertical gradient is related to the progressive hydration of the samples. The numerical predictions for tests WP5_1B, C_1, C_2 and C_6 present this behaviour with a good agreement between experimental and numerical results for tests WP5_1B and C_1 (despite the difference in initial dry density for this latter one). However, discrepancies between experimental results and numerical prediction are found in tests C_2 and C_6.

As already mentioned, with respect to test C_2 (Fig. 17), experimental outcomes underline a generalized volume increase, which contradicts the hypothesis of constant volume hydration. On the contrary, numerical predictions highlight an expected swelling in proximity of the wetting surfaces (top and bottom here) and the consequential compaction of the central part.

For test C_6, the dry density and water content gradient simulated by the numerical predictions do not correspond to the experimental results, which are strongly affected by the experimental radial gap. Indeed, a homogeneous dry density distribution for the experimental test can be observed, which suggests that the swelling upon hydration has mainly occurred in the radial direction.

The experimental compacted bentonite volume increase occurs in the radial gap rather than compacting the sample portion located in the opposite hydration location, as the numerical model reproduces, generating a quasi-homogeneous dry density distribution. The water content profiles (Fig. 18) are precisely related to the dry density distributions and full saturated states.

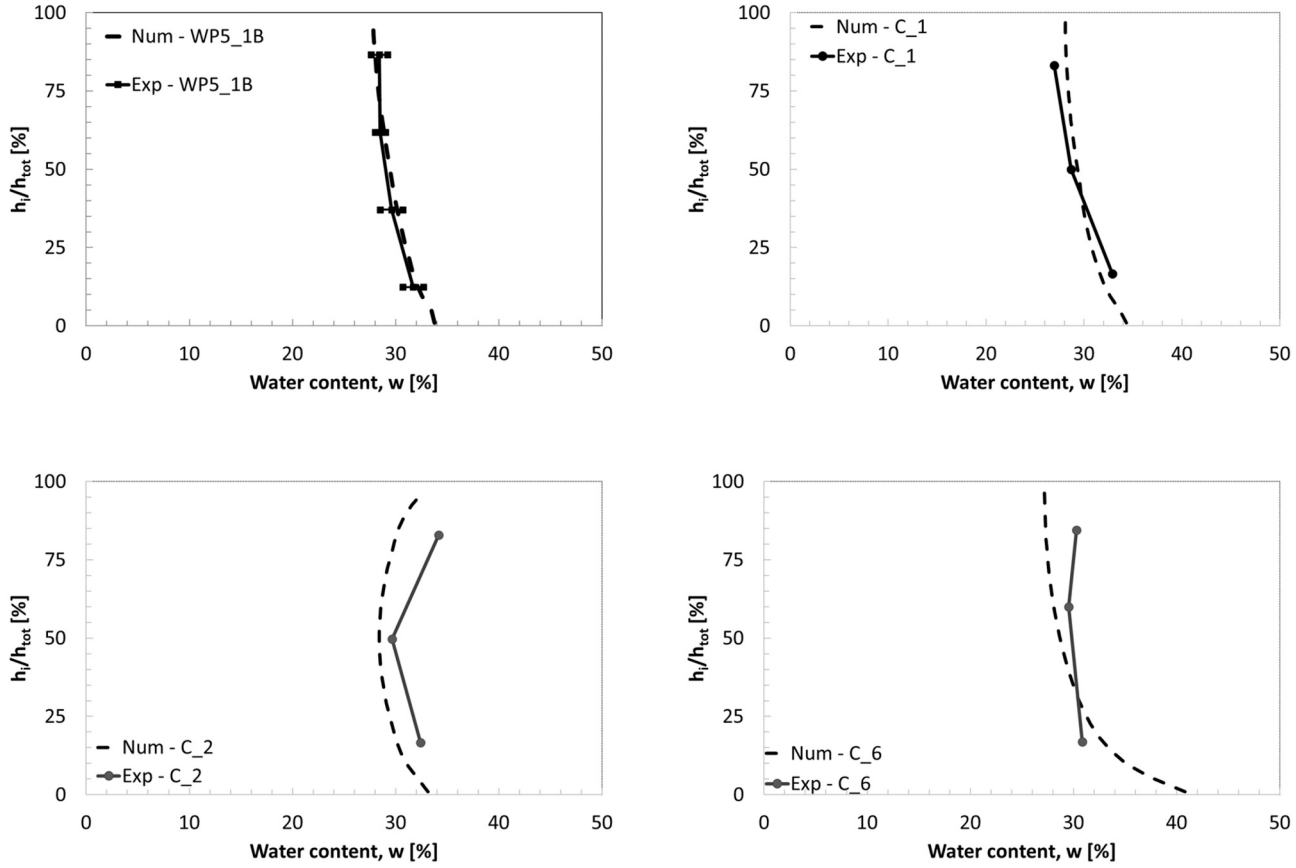

Fig. 18. Water content distribution over the height of the sample at the end of the test for tests WP5_1B, C_1, C_2 and C_6. Comparisons between experimental data and model predictions.

8.3. *Mercury intrusion porosimetry*

The experimental campaign included Mercury Intrusion Porosimetry (MIP) measurements performed on freeze-dried samples taken from tests WP5_1B, C_1 and C_2 after dismantling (Fig. 19 shows results from tests WP5_1B and C_2) and also measurements on the initial state of the material, i.e. pellets and powder (Bernachy-Barbe, 2020). At the initial state, the single pellet presents a predominant pore family with a very small pore entry diameter (between 10 and 20 nm), whereas the crushed pellets-powder mixture is characterized by a similar fine porosity plus a predominant pore entry diameter which is 5 orders of magnitude larger.

After saturation all the analysed tests present a first peak value in proximity of a pore entry diameter equal to d = 20 nm (close to the pellet pore size value), which has a contribution to the total porosity similar to the pellets in initial state. A second peak value is observed at d = 50 μm (remarkably smaller with respect to the initial pore size dominating the crushed pellets pore structure). Conversely from test WP5_1B, test C_2 presents an additional pore family with a peak corresponding to the pore entry diameter equal to d = 200 nm, just in between the above-mentioned pore families. Those additional pore families are detected close to the wetting surfaces (top and bottom for test C_2), where the lowest dry density is observed during the post mortem analysis (Fig. 17). The very large pores observed in the initial crushed powder have disappeared and are transformed in pores of diameter around 200 nm and

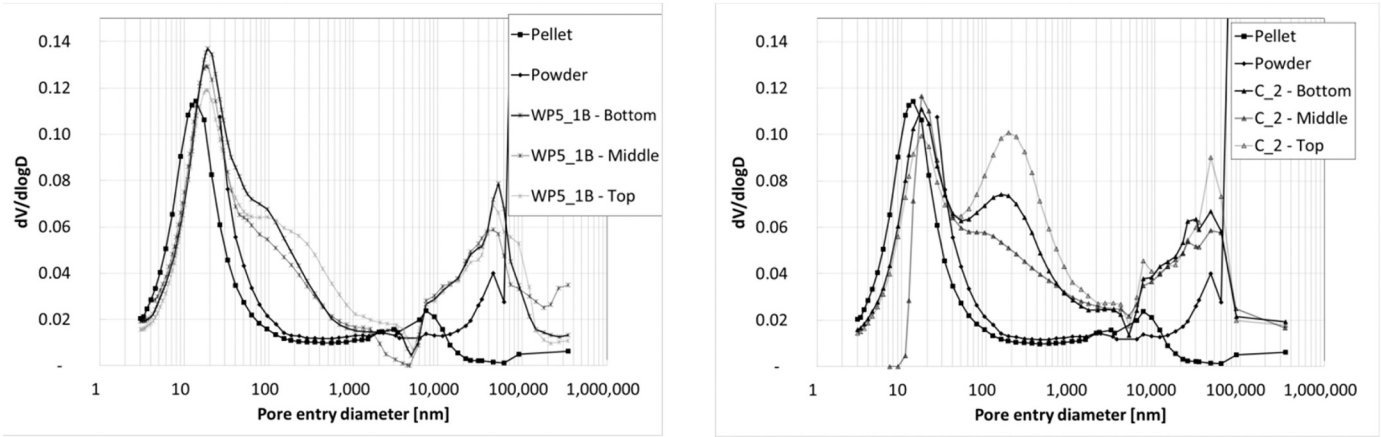

Fig. 19. MIP characterisation of single pellets and powder at initial state and for tests WP5_1B and C_2 at several sample heights at the end of the tests.

around 50 μm.

MIP experimental results on pellets mixtures present comparable features as the ones found by (Seiphoori et al., 2014) on compacted MX-80 pure bentonite and (Wang et al., 2014) on MX-80 and sand compacted mixture after saturation.

Although several authors (Wang et al., 2013), (F. Zhang et al., 2018), (Seiphoori et al., 2014) propose possible quantitative distinctions and thresholds between the *larger pore diameter families* and *smaller pore diameter families* with respect to different criteria, it is evident that the strongly coupled multi-structural and multi-physics phenomena modifying these distributions do not allow a unique and abrupt separation between structures.

Indeed, the presented experimental results show how in test C_2 an additional pore family appears just in between the larger and smaller diameter structures at the end of the test.

Moreover, different authors refer indiscriminately to different pore diameter structures with the same definition and with different definitions to the same pore diameter structure, leading incontrovertibly to misunderstandings.

Consequentially, in this work, the definition of micro and macro porosity has not been used when commenting experimental results, but the wordings "large pore diameter structures" and "small pore diameter structures" was preferred. In contrast to other distinctions, this separation is straightforward thanks to the fact that the dominating pores families diameters span several orders of magnitude. Nevertheless, a unique distinction between large pores diameter structures and small pores diameter structures was necessary and unavoidable when dealing with the numerical modelling, as it is showed with reference to numerical results of water retention behaviour (3.2) and permeability evolution (7.2).

9. Conclusions

This work presented isochoric-wetting tests performed on a MX80 bentonite in the form of different assemblies (i.e. 32-mm pellets mixture, 7 mm-pellets mixtures and isotropic compacted block surrounded by radial gap) with similar dry densities and different hydration lengths. The considered experimental tests present initially very heterogeneous pore structures and dry density distributions, which evolve toward homogenised structures. This feature affects the swelling pressure development and water transfer mechanisms.

Firstly, it is possible to see that the elastic swelling pressure develops with a higher rate in compacted bentonite samples (test C_6) with respect to pellets mixtures samples (tests WP5_1B, C_1 and C_2).

Secondly, after reaching the pre-consolidation pressure (yield locus), it is observed that the pore structure distribution of a compacted bentonite sample does not present enough microstructural swelling strain to compensate for collapse deformation. Differently from pellets mixtures, test C_6 presents a load sufficiently high that causes the collapse of the macro-structure. The successive vertical stress decrease is due to the compensation for the collapse compressive strain.

Although the proposed numerical approach does not take into account the distinctions between pore diameter structures and their distributions, the numerical results underline a good agreement with experimental measurements. Especially, the non-monotonic evolution of the axial swelling pressure is well captured for all the tests.

Discrepancies between numerical predictions and experimental results are found for the radial pressure development of test C_6. Those are related to the experimental radial gap partially filled with bentonite powder, which is not considered in the numerical modelling. The post mortem analyses comparisons between experimental results and numerical predictions also show similar features. These comparisons allow detecting experimental uncertainties (i.e. dry density experimental evaluation for test C_2) and the limits of numerical simplifications (i.e. numerical dry density vertical gradient vs homogeneous dry density vertical experimental profile for test C_6). With respect to test C_6, it is possible to underline how the position of the large pore diameter structure (i.e. gap partially filled with loose powder in the radial direction) with respect to the small pore diameter structure (i.e. central compacted bentonite sample) plays an essential role concerning swelling pressure development and final state performances assessments (i.e. dry density and permeability distributions). With respect to this, numerical modelling simplifications should always be taken with caution.

Finally, a numerical approach is presented and adopted in order to evaluate the permeability evolution of large pore diameter structures. The results of this experimental evaluation are compared to other experimental records (i.e. swelling pressure, water intake and suction) underlining and confirming a strongly coupled hydro-mechanic and multi-porosity processes characterising the unsaturated swelling clays.

It can be concluded that this model allows making numerical simulations of a number of experimental results at different scales with remarkable results as shown profoundly in (Gramegna, 2021), thus allowing accurate predictions of material behaviour in several conditions.

Funding

This work was funded by the European project BEACON (project receiving funding from the Euratom research and training programme 2014–2018 under grant agreement No 745942 and the Agence Nationale de gestion des Déchets Radioactifs (Andra).

CRediT authorship contribution statement

Liliana Gramegna: Conceptualization, Formal analysis, Validation, Writing – original draft. **Fabien Bernachy-Barbe:** Investigation. **Frédéric Collin:** Writing – review & editing, Supervision. **Jean Talandier:** Funding acquisition, Writing – review & editing. **Robert Charlier:** Supervision, Writing – review & editing.

Declaration of Competing Interest

The authors declare that they have no known competing financial interests or personal relationships that could have appeared to influence the work reported in this paper.

References

Alonso, E.E., Gens, A., Josa, A., 1990. A Constitutive Model for Partially Saturated Soils. Géotechnique 40 (3), 405–430.

Alonso, E.E., Hoffmann, C., Romero, E., 2010. Pellet Mixtures in Isolation Barriers. J. Rock Mech. Geotech. Eng. 2 (1), 12–31. https://doi.org/10.3724/SP.J.1235.2010.00012.

Baryla, P., et al., 2018. Bentonite Mechanical Evolution – Experimental Work for the Support of Model Development and Validation. Technical Report - BEACON Project.

Bernachy-Barbe, F., 2020. "Homogenization of Bentonite upon Resaturation: Density and Pressure Fields." (Under peer review).

Bernachy-Barbe, F., 2021. Homogenization of bentonite upon saturation: density and pressure fields. Appl. Clay Sci. 209, 106122.

Bernachy-Barbe, F., Conil, N., Guillot, W., Talandier, J., 2020. Observed Heterogeneities after Hydration of MX-80 Bentonite under Pellet / Powder Form. Appl. Clay Sci. 189 https://doi.org/10.1016/j.clay.2020.105542.

Cui, Y.J., 2017. On the hydro-mechanical behaviour of MX80 bentonite-based materials. J. Rock Mech. Geotech. Eng. 9 (3), 565–574. https://doi.org/10.1016/j.jrmge.2016.09.003.

Dardé, B., et al., 2018. Hydro-mechanical behaviour of high-density bentonite pellet upon partial hydration. Geotech. Lett. 8 (4), 1–23.

Dardé, B., et al., 2019. "Experimental and Numerical Study of the Hydromechanical Behaviour of Bentonite Pellet-Powder Mixtures." Ph.D. thesis. École des Ponts ParisTech.

Darde, B., et al., 2020. Effects of the initial granular structure of clay sealing materials on their swelling properties: experiments and DEM simulations. EPJ Nuclear Sci. Technol. 6, 1.

Delage, P., Cui, Y.J., Tang, A.M., 2010. Clays in Radioactive Waste Disposal. J. Rock Mech. Geotech. Eng. 2, 111–123.

Dieudonné, A.C., Della Vecchia, G., Charlier, R., 2017. Water Retention Model for Compacted Bentonites. Can. Geotech. J. 54 (7), 915–925.

Dueck, A., Nilsson, U., 2010. Tr-10-55 *Thermo-Hydro-Mechanical Properties of MX-80.* Results from Advanced Laboratory Tests. Technical Report - SKB.

Gramegna, L., 2021. Hydromechanical Behaviour of Bentonite Sealings in the Context of Nuclear Waste Disposals: Contributions for Engineered Barriers Evaluation. University of Liege.
Imbert, C., Villar, M.V., 2006. Hydro-Mechanical Response of a Bentonite Pellets / Powder Mixture upon Infiltration. Appl. Clay Sci. 32, 197–209.
Liu, Z.R., et al., 2019. Particle size Ratio and distribution Effects on Packing Behaviour of Crushed GMZ Bentonite Pellets. Powder Technol. 351, 92–101. https://doi.org/10.1016/j.powtec.2019.03.038.
Liu, Z.R., Cui, Y.J., Ye, W.M., Chen, B., et al., 2020a. Investigation of the Hydro-Mechanical Behaviour of GMZ Bentonite Pellet Mixtures. Acta Geotech. 15 (10), 2865–2875. https://doi.org/10.1007/s11440-020-00976-y.
Liu, Z.R., Cui, Y.J., Ye, W.M., Zhang, Z., et al., 2020b. Investigation on Vibration Induced Segregation Behaviour of Crushed GMZ Bentonite Pellet Mixtures. Constr. Build. Mater. 241, 117949. https://www.sciencedirect.com/science/article/pii/S0950061819334026.
Lloret, A., et al., 2003. Mechanical behaviour of heavily compacted bentonite under high suction changes. Géotechnique 53 (1), 27–40. http://www.icevirtuallibrary.com/doi/10.1680/geot.2003.53.1.27.
Molinero, A., et al., 2017. In-Depth characterisation of a mixture composed of powder / pellets MX80 bentonite. Appl. Clay Sci. 135, 538–546.
Molinero, A., et al., 2019. Characterization of water retention, compressibility and swelling properties of a pellet / powder bentonite mixture. Eng. Geol. 248, 14–21. https://doi.org/10.1016/j.enggeo.2018.11.005.
Navarro, V., et al., 2020. From double to triple porosity modelling of bentonite pellet mixtures. Eng. Geol. 274 (April), 105714 https://doi.org/10.1016/j.enggeo.2020.105714.
Pusch, R., 1979. Highly compacted sodium bentonite for isolating rock-deposited radioactive waste products. Nucl. Technol. 45, 153–157.
Romero, E., 2013. A microstructural insight into compacted clayey soils and their hydraulic properties. Eng. Geol. 165, 3–19.
Romero, E., Della Vecchia, G., Jommi, C., 2011. An insight into the water retention properties of compacted clayey soils. Géotechnique 61 (4), 313–328. http://www.icevirtuallibrary.com/doi/10.1680/geot.2011.61.4.313.
Seiphoori, A., Ferrari, A., Laloui, L., 2014. Water retention behaviour and microstructural evolution of mx-80 bentonite during wetting and drying cycles. Géotechnique 64 (9), 721–734. http://www.icevirtuallibrary.com/doi/10.1680/geot.14.P.017.
Sellin, P., Leupin, O.X., 2014. The use of clay as an engineered barrier in radioactive-waste management - a review. Clay Clay Miner. 61 (6), 477–498.
Sellin, P., et al., 2020. Beacon: bentonite mechanical evolution. EPJ Nuclear Sci. Technol. 6, 23.
Talandier, J., 2018. Specifications for BEACON WP5: Testing, Verification and Validation of Models Step 1- Verification Cases. Technical Report - BEACON Project.
Tang, A.M., Cui, Y.J., Barnel, N., 2008. Thermo-mechanical behaviour of a compacted swelling clay. Géotechnique 58 (1), 45–54.
Wang, Q., et al., 2013. Hydraulic conductivity and microstructure changes of compacted bentonite / sand mixture during hydration. Eng. Geol. 164, 67–76. https://doi.org/10.1016/j.enggeo.2013.06.013.
Wang, Q., et al., 2014. Time- and density-dependent microstructure features of compacted bentonite. Soils Found. 54 (4), 657–666.
Zhang, Z., et al., 2015. Mechanical behavior of GMZ bentonite pellet mixtures over a wide suction range. Appl. Clay Sci. 23 (1–4), 325–336. https://doi.org/10.1016/j.clay.2015.10.015.
Zhang, F., Cui, Y.J., Ye, W.M., 2018. Distinguishing macro- and micro-pores for materials with different pore populations. Geotech. Lett. 8, 1–9.